AD-A087 959 SOLAR TURBINES INTERNATIONAL SAN DIEGO CA F/G 11/2
STUDY OF EROSION MECHANISMS OF ENGINEERING CERAMICS, STATIC FAT--ETC(U)
JUL 80 M E GULDEN N00014-73-C-0401
UNCLASSIFIED NL

1 OF 1
AD A
087959

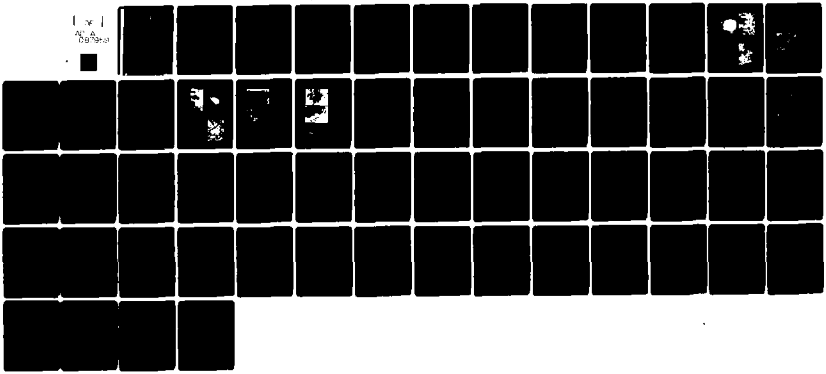

STUDY OF EROSION MECHANISMS OF ENGINEERING CERAMICS

Static Fatigue of Ceramics

by M.E. Gulden

SOLAR TURBINES INTERNATIONAL
An Operating Group of International Harvester
2200 Pacific Highway, P.O. Box 80966,
San Diego, California 92138

31 July 1980

Final Report for Period 1 April 1973 - 1 January 1980

Prepared for

Office of Naval Research
Department of the Navy
Arlington, Virginia 22217

UNCLASSIFIED

SECURITY CLASSIFICATION OF THIS PAGE (*When Data Entered*)

REPORT DOCUMENTATION PAGE

READ INSTRUCTIONS BEFORE COMPLETING FORM

~~1. REPORT NUMBER~~

6

Study of Erosion Mechanisms of

[redacted]F ENGINEERING CERAMICS

Static Fatigue of Ceramics

2. GOVT ACCESSION NO. AD-A087959

3. RECIPIENT'S CATALOG NUMBER

~~5. TYPE OF REPORT~~ & PERIOD COVERED

9

Final Report,

1 Apr[redacted]73-Jan[redacted]980

~~6. PERFORMING ORG. REPORT NUMBER~~

1

~~7. AUTHOR(s)~~

10

Mary Ellen Gulden

15

8. CONTRACT OR GRANT NUMBER(s)

N00014-73-C-0401

9. PERFORMING ORGANIZATION NAME AND ADDRESS

Solar Turbines International
2200 Pacific Highway, P.O. Box 80966
San Diego, California 92138

10. PROGRAM ELEMENT, PROJECT, TASK AREA & WORK UNIT NUMBERS

NR032-542

11. CONTROLLING OFFICE NAME AND ADDRESS

Department of the Navy
Office of Naval Research
Arlington, Virginia 22217

31

~~12. REPORT DATE~~

Jul[redacted]980

13. NUMBER OF PAGES

55

14. MONITORING AGENCY ~~NAME & ADDRESS~~(if different from Controlling Office)

12

58

15. SECURITY CLASS. (*of this report*)

Unclassified

15a. DECLASSIFICATION DOWNGRADING SCHEDULE

16. DISTRIBUTION STATEMENT (*of this Report*)

Distribution of this document is unlimited.

This [illegible]
fo[illegible]
distribution [illegible]

17. DISTRIBUTION STATEMENT (*of the abstract entered in Block 20, if different from Report*)

18. SUPPLEMENTARY NOTES

19. KEY WORDS (*Continue on reverse side if necessary and identify by block number*)

Dust Erosion	Magnesium Fluoride
Solid Particle Impact	Alumina
Silicon Nitride	Stress Corrosion
Silicon Carbide	Static Fatigue

20. ABSTRACT (*Continue on reverse side if necessary and identify by block number*)

Two areas were investigated in this program: solid particle erosion of engineering ceramics and static fatigue of ceramics.

In the erosion phase, the target materials investigated were several types of Si_3N_4, glass bonded Al_2O_3 and magnesium fluoride. The particle types were SiC and natural quartz sand. Particle sizes ranged between 10 and 1000 microns and particle velocities were in the subsonic regime. The particle size and velocity dependence on erosion, effect of erosion on strength and effect of number of

DD FORM 1 JAN 73 1473

UNCLASSIFIED

SECURITY CLASSIFICATION OF THIS PAGE (*When Data Entered*)

impacts on erosion were determined. It was found that the type of erosion damage produced was more a function of relative target particle properties than of particle size and velocity for the erosion regime investigated. "Elastic-plastic" impact, which is characterized by plastic deformation in the particle contact area, and radial and lateral cracks propagating outward from the contact area was observed on all targets impacted with SiC particles. Damage from quartz particle impact ranged from elastic-plastic on the relatively soft targets like MgF_2 to shallow intergranular chipping with no secondary crack formation for the hard targets such as hot-pressed Si_3N_4.

Static fatigue behavior of four ceramics was determined in various aqueous solutions at temperatures to 900°C. Hot-pressed Si_3N_4 did exhibit time-dependent failure and strength decreased with increase in available moisture. The glassy grain boundary phase is thought to be responsible for this behavior. Reaction bonded Si_3N_4 which does not contain a glassy phase did not exhibit time-dependent failure. A model was proposed for the mechanism of stress corrosion of hot-pressed Si_3N_4 based on ion exchange occurring in the glassy grain boundary phase.

TABLE OF CONTENTS

APPENDICES

LIST OF FIGURES

LIST OF TABLES

1

INTRODUCTION

This final report summarizes research for the Office of Naval Research under Contract N00014-73-C-0401, performed in the period from April 1973 through January 1979. Work was directed toward two principal areas: erosion mechanisms of ceramics and static fatigue of ceramics. The experimental approach has been to perform controlled experiments on ceramics of engineering interest which not only promotes basic understanding of behavior, but also generates data of direct use to engineered components.

Accomplishments under the contract have been reported in seven technical reports, six* publications in the open literature and five oral presentations. These are listed in Table 1. The results can be conveniently separated into six phases as follows:

Phase I	-	Erosion of Si_3N_4 Materials
Phase II	-	Correlation of Experimental Erosion Data with Elastic-Plastic Impact Models
Phase III	-	Effect of Number of Impacts on Erosion in the Elastic-Plastic Response Regime
Phase IV	-	Erosion of a Two-Phase Target - Alsimag 614 Al_2O_3
Phase V	-	Effect of Erosion on Strength
Phase VI	-	Static Fatigue of Ceramics

Each phase will be discussed separately in Section 2. The first two phases have not been published previously and will be discussed in detail. Results from the remaining phases have been published in technical reports and the open literature and will be summarized in this report. The experimental procedure and test equipment is described in Appendix A and erosion data is given in Appendix B.

---

* Two to be published

Table 1

Publications and Presentations

Publications

1. "Stress Corrosion of Silicon Nitride", J. Am. Cer. Soc., 59, p. 391, 1976.
2. "Impact Damage in Brittle Materials in the Elastic-Plastic Response Regime", Proc. Roy. Soc. Series A, 361, p. 343, 1978
3. "Solid Particle Erosion of High-Technology Ceramics (Si_3N_4, Glass-Bonded Al_2O_3 and MgF_2)", ASTM - STP 664 Erosion: Prevention and Useful Applications, p. 101, 1979.
4. "Effect of Number of Impacts on Erosion of Polycrystalline MgF_2 in the Elastic-Plastic Response Regime", J. Am. Cer. Soc., p. 121, 1980.
5. "Solid Particle Erosion of Si_3N_4 Materials", to be published in Wear.
6. "Correlation of Erosion Data with Elastic-Plastic Impact Models", to be published in J. Am. Cer. Soc.

Technical Reports

1. Static Fatigue of Ceramic Materials, Feb. 1974.
2. Static Fatigue of Ceramic Materials, July 1974.
3. Stress Corrosion of Si_3N_4, May 1975.
4. Study of Erosion Mechanisms of Engineering Ceramics, Apr. 1976.
5. Study of Erosion Mechanisms of Engineering Ceramics, Apr. 1977.
6. Study of Erosion Mechanisms of Engineering Ceramics, Aug. 1977.
7. Effect of Number of Impacts on Erosion in the Elastic-Plastic Response Regime, Mar. 1979.

Presentations

1. "Static Fatigue of Silicon Nitride", Program Review for ONR/NASC contracts on Silicon Nitride as a Bearing Material, King of Prussia, PA, 1974.
2. "Erosion Mechanisms of Brittle Materials", ONR Contractors Meeting on Impact Response and Erosion Mechanisms for Brittle Materials, La Jolla, CA, 1975.
3. "Stress Corrosion of Silicon Nitride", Am. Cer. Soc. Reg. Meeting, San Francisco, CA, Oct. 1976.
4. "Solid Particle Erosion of High Technology Ceramics, ASTM Symposium", Erosion: Prevention and Useful Applications, Vail, CO, Oct. 1977.
5. "Erosion of Si_3N_4 Materials", Am. Cer. Soc. Reg. Meeting, San Diego, CA, Oct. 1978.

2

RESEARCH ACCOMPLISHMENTS

2.1 PHASE I - EROSION OF Si_3N_4 MATERIALS

2.1.1 Introduction

The purpose of this phase of the investigation was to determine the effects of microstructural variation on erosion and incorporate these effects into the elastic-plastic impact models. A second objective was to further elucidate the conditions (particle size and velocity, relative target and particle properties) where elastic-plastic impact occurs. Elastic-plastic impact damage is characterized by a heavily deformed contact area between particle and target, with radial cracks propagating outward from the contact zone, and with subsurface lateral cracks propagating outward on planes nearly parallel to the surface (Ref. 1). The elastic-plastic models, based on isotropic materials and single impacts, predict that erosion is a function of particle size, velocity and density; and target density, hardness and fracture toughness.

2.1.2 Materials and Test Procedure

Four commercially available silicon nitride materials were selected for target materials. Although the targets do not provide a systematic variation in microstructure, they do cover a wide range of structure and properties. The target materials and relevant mechanical properties are shown in Table 2. Four-point bend strength is not specifically related to erosion resistance, but is included in Table 2 to illustrate the large variation in mechanical properties encompassed by these targets. Properties of the impacting particles are also included in Table 2. Microstructure of the targets is shown in Figures 1 and 2. Hot-pressed Si_3N_4 is fine grained, fully dense and contains minor amounts of glassy phase at the grain boundaries. The pressureless sintered material is also fine grained but contains significant amounts of glassy phase at the grain boundaries and isolated regions of small porosity and second phase particles of silicon and molybdenum silicide. Both of the reaction bonded materials are approximately 75 percent dense. However, the porosity in the NC350 product is relatively small (1-7 microns) and uniformly distributed. The KBI product is very inhomogeneous and contains non-uniform porosity as large as 50 microns, unreacted silicon regions as large as 60 microns and other second phase particles.

Table 2

Si_3N_4 Target and Particle Properties

	Elastic Modulus (GPa)	Fracture Toughness ($MPam^{1/2}$)	Hardness (GPa)	Four-Point Bend Strength (MPa)
Hot-pressed (NC132)	320	5	16	725
Pressureless sintered (GTE 3502)	255	6	12	450
Reaction bonded (NC 350)	170	2.2	7.5	210
Reaction Bonded (KBI)	147	2.2	5	145
Quartz	95	0.7	6	
SiC	420	3	23	

The particles selected for impact and erosion testing also provide a variation in properties. SiC is harder than all of the targets, while quartz is softer than hot-pressed and pressureless sintered Si_3N_4 and has equivalent hardness to the two reaction bonded materials.

Six narrow size ranges between 10 and 385 microns average quartz and 8 to 940 microns average SiC particles were used. For each particle size up to five velocities between 24 and 285 m/sec were evaluated.

2.1.3 Erosion Weight Loss and Particle Size and Velocity Dependencies

Erosion weight loss at 90-degree impingement was measured on the four targets for impact with both SiC and natural quartz (SiO_2) particles. The erosion dependence on particle size and velocity was determined. The exponential functions are shown in Tables 3 and 4. For impact with SiC particles, erosion per impact of all targets was dependent on particle radius to the fourth power for all velocities. The radius exponent for quartz particle impact varied between three for hot-pressed Si_3N_4 to approximately four for the other targets. The power function for velocity dependence on erosion was not as consistent and varied from one for hot-pressed Si_3N_4 impacted with all particle sizes of quartz to as high as six for NC350 reaction bonded Si_3N_4 impacted with quartz, although the most common value was between three and four. Except for hot-pressed Si_3N_4 impacted with quartz, there was not a consistent variation in velocity exponent with target material, particle size or particle type. To compare erosion weight loss of the four targets the data was plotted as erosion volume loss/ impact versus particle radius

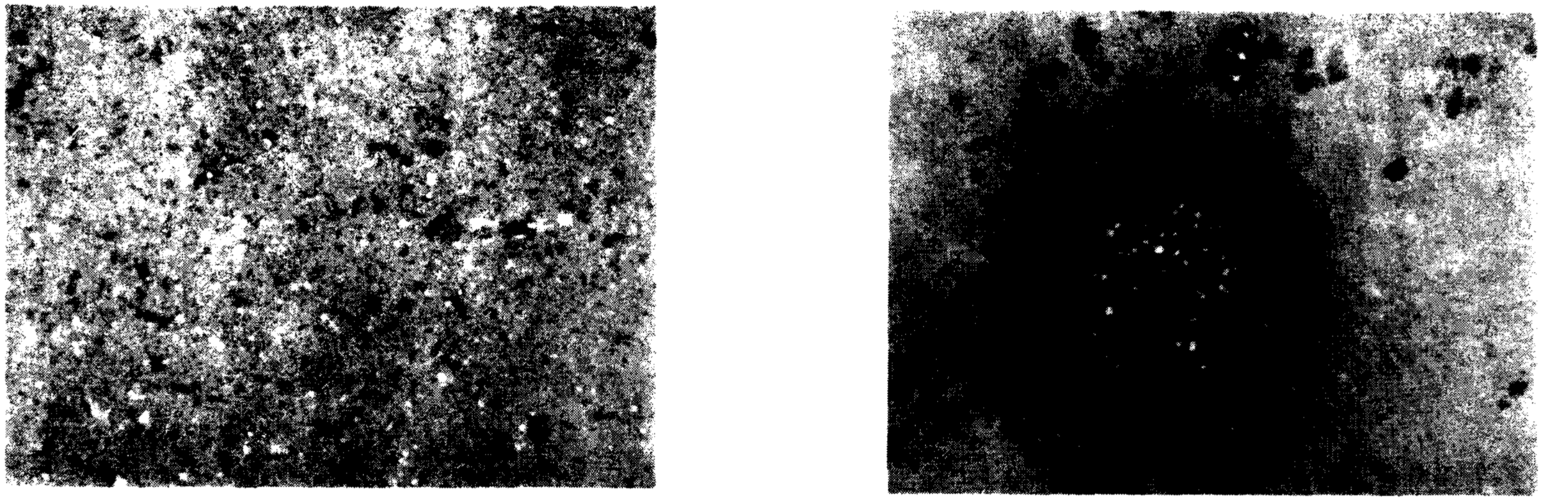

Hot Pressed (NC 132)

Pressureless Sintred (GTE 3502)

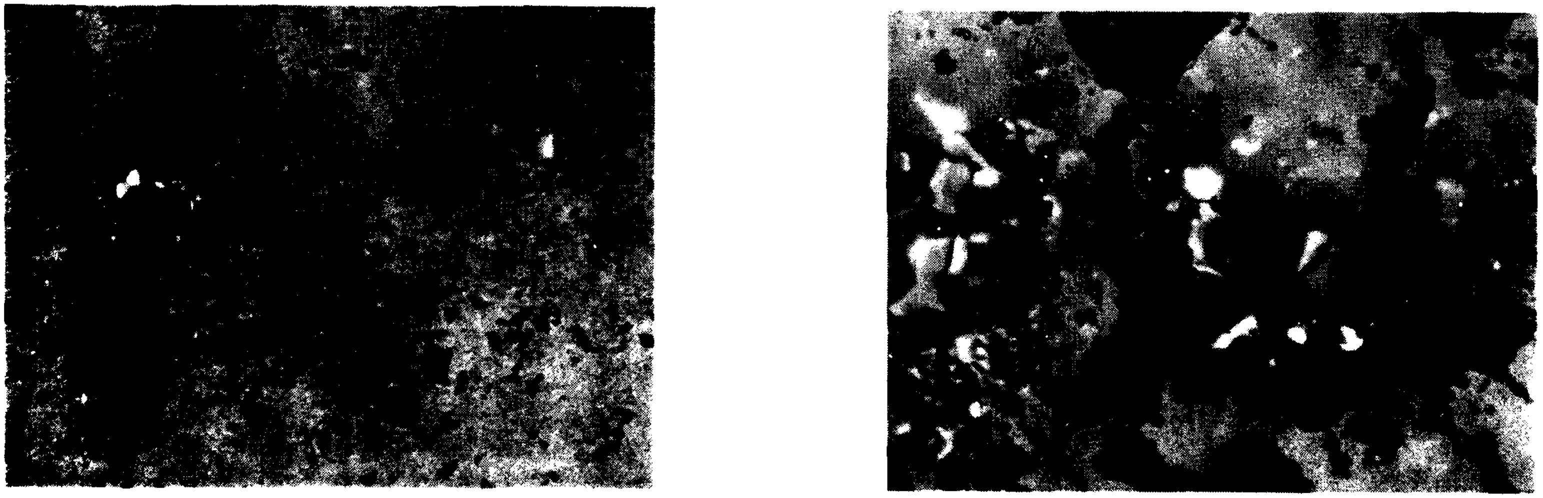

Reaction Bonded (NC 350)

Reaction Bonded (KBI)

Figure 1. Microstructure of Target Materials
Magnification: 1000X

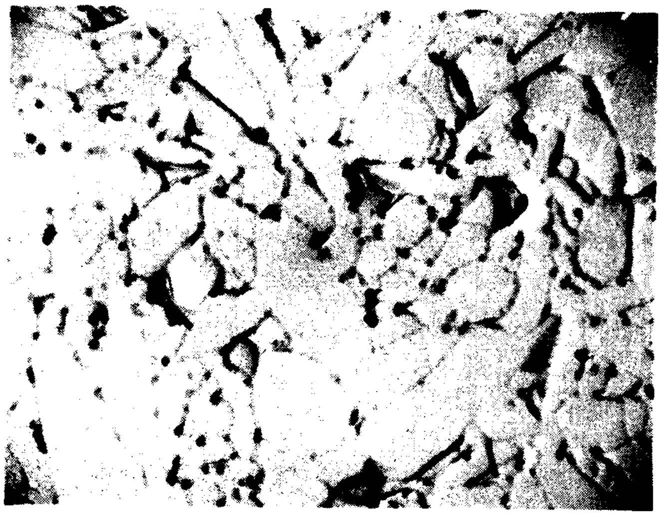

Hot Pressed (NC 132)

Pressureless Sintered (GTE) 3502

Figure 2. Etched Microstructure of Hot Pressed and Pressureless Sintered Si_3N_4
Magnification: 12,000X

Table 3

Exponential Function for Particle Size Dependence on Erosion of Si_3N_4

	Quartz Particle Velocity (mps)			SiC Particle Velocity (mps)		
	80	160	250	50	100	150
NC 132	3.1	3.1	3.2	4.1	4.0	4.1
GTE 3502	-	3.9	3.9	4.0	3.9	4.0
NC 350	3.4	4.1	4.5	4.1	4.3	4.4
KBI	3.9	4.0	4.2	3.9	3.9	3.9

Table 4

Exponential Function for Particle Velocity Dependence on Erosion of Si_3N_4

	Quartz Particle Size (microns)						SiC Particle Size (microns)					
	385	273	115	64	49	10	940	560	305	102	50	8
NC 132	-	1.1	1.1	1.1	1.0	1.0	3.1	4.1	4.9	3.0	5.6	3.6
GTE 3502	2.6	1.7	2.5	-	-	-	2.9	-	3.4	3.1	-	2.8
NC 350	5.8	4.8	2.9	3.4	3.9	4.3	4.1	-	3.0	2.9	-	2.1
KBI	3.1	2.9	2.8	-	-	2.4	2.5	-	2.8	3.1	-	2.9

to the fourth power (R^4) times velocity to the third power (V^3). This is shown in Figures 3 and 4. As can be seen in Figure 3, for impact with SiC particles, the data fit reasonably well on two parallel lines of slope = 1 for all particle sizes and velocities, suggesting the same mechanism is operative for this range of particle size and velocities. Erosion loss for the two reaction bonded targets is indistinguishable, as is that for the hot-pressed and pressureless sintered targets; and they are separated by approximately one order of magnitude of volume loss/impact for the same particle size-velocity test condition. There is less difference between the targets for impact with 8 micron particles. This is thought to be due to embedding of the small particles in the pores of the reaction bonded materials which, in effect, reduces the measured weight loss. (Examination of the eroded surfaces does reveal embedding of 8 micron particles, which does not occur significantly with the larger particles.) Erosion for quartz particle impact versus R^4V^3 is shown in Figure 4. Data for the reaction bonded targets fits a straight line relation of slope 1 (log.log basis) fairly well. However, there is a separation in volume loss of approximately one order of magnitude between the two targets for the same impact conditions.

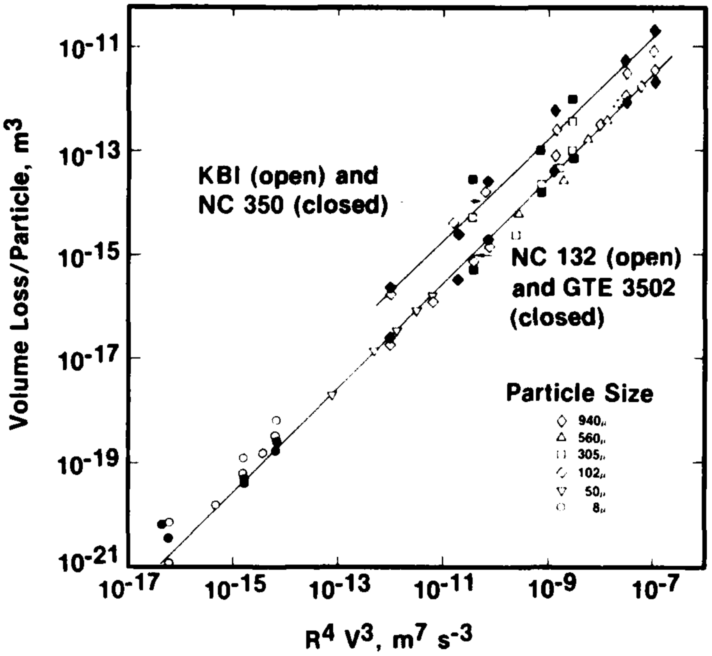

Figure 3. Erosion of Four Si_3N_4 Materials Impacted with SiC Particles

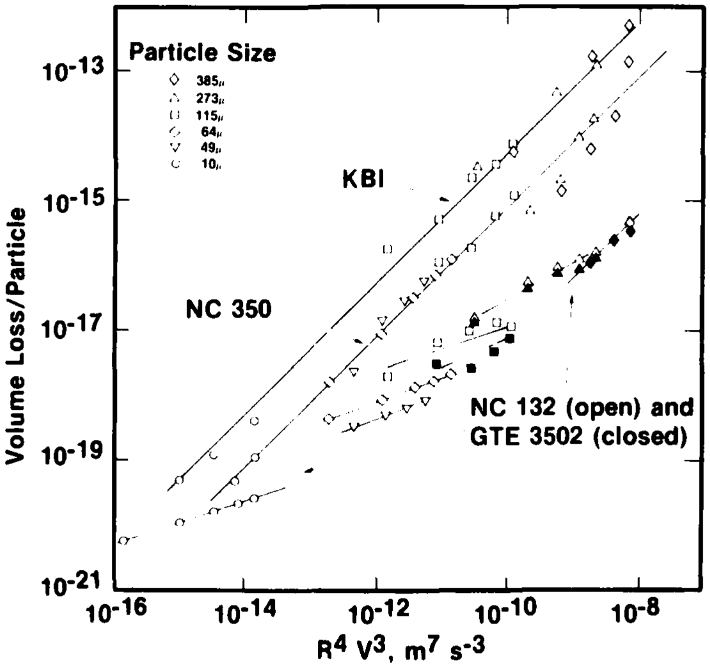

Figure 4. Erosion of Four Si_3N_4 Materials Impacted with Quartz Particles

The erosion data for hot-pressed and pressureless sintered Si_3N_4 do not follow a straight line relationship, which is due primarily to the lower velocity exponent dependence on erosion (Table 4) for these targets. Again, for a given particle size-velocity test condition, erosion weight loss was the same for hot-pressed and pressureless sintered Si_3N_4. At higher velocities there are several orders of magnitude difference between reaction bonded and sintered (both pressureless sintered and hot-pressed Si_3N_4). The data suggest there is a change in erosion mechanism for impact with quartz particles on hot-pressed and pressureless sintered Si_3N_4. The data further suggest that the relative target/particle properties are more important with regard to controlling erosion mechanism than variation in particle size and velocity for the test conditions investigated.

2.1.4 Characterization of Erosion Damage

Both heavily eroded surfaces and single impacts were examined to characterize damage and material removal processes. All targets impacted with SiC particles exhibited elastic-plastic type impact damage (Ref. 1). Typical examples for each target are shown in Figure 5. Although all of the targets impacted with SiC particles exhibited elastic-plastic impact, there was minor variation in the damage. Details of impact damage are shown in Figure 6. Figure 5A shows single impact damage on hot-pressed Si_3N_4. The radial and lateral cracks are long and tight. None of the laterally cracked material in this example has been removed. The secondary cracks on the pressureless sintered target are more open and intergranular or through the glassy grain boundary phase, Figure 5B and 6A. The radial cracks in the hot-pressed Si_3N_4 were transgranular, but the lateral cracks were intergranular. Cracking in NC350 reaction bonded Si_3N_4 was wide and followed the porosity. Crack branching was observed. The impact area in KBI reaction bonded Si_3N_4 (Fig. 5C) was relatively large and secondary cracks, both lateral and radial, were minimized (Fig. 5D). It was difficult to differentiate impact areas from the large pores inherent in this target. The appearance of the actual impact areas for all the targets impacted with SiC was not one of brittle fracture, but rather of plastic flow. No cleavage markings or intergranular facets were observed. A typical example of the bottom of an impact crater is shown in Figure 6B.

The impact damage produced by quartz particles was quite different from that produced by SiC particles. The damage produced on hot-pressed and pressureless sintered Si_3N_4 was characterized by shallow intergranular chipping, as shown in Figure 7A and B and no cracking was observed away from the impact area. The damage on NC350 reaction bonded Si_3N_4 was characterized by concentric ring cracks. This type of damage has been observed previously, usually under low velocity or static impact, and is considered to be due to elastic interaction between particle and target. On the KBI reaction bonded Si_3N_4, the quartz particle impacts were not distinguishable from the porosity.

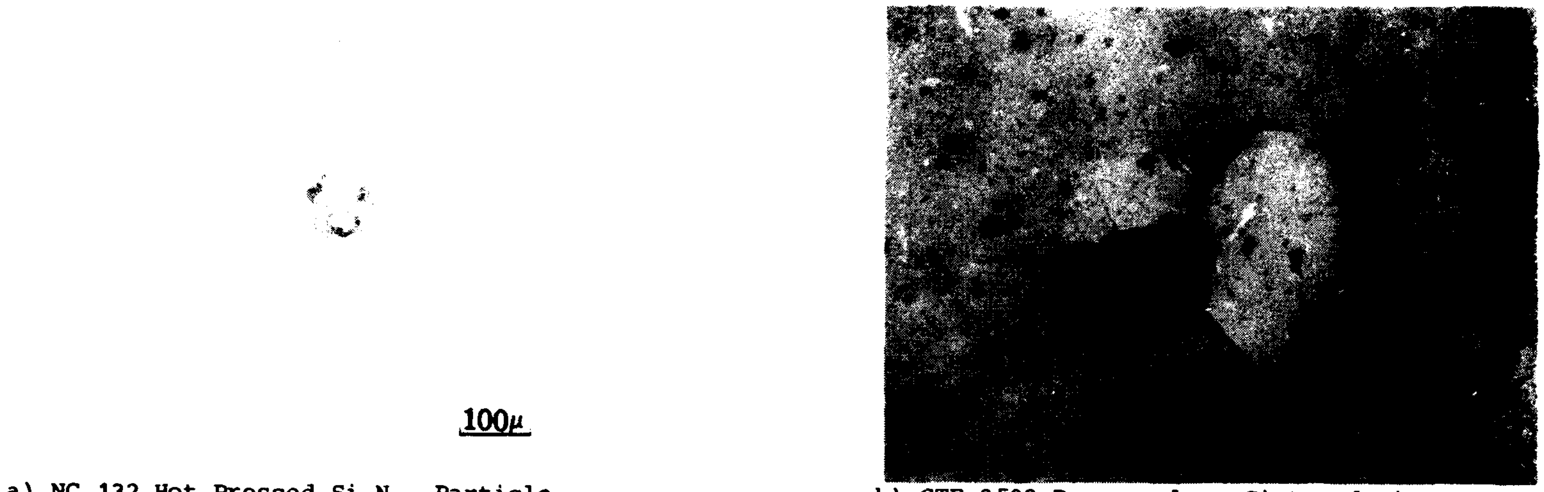

a) NC 132 Hot Pressed Si_3N_4. Particle Velocity = 176 mps

b) GTE 3502 Pressureless Sintered Si_3N_4. Particle Velocity = 176 mps

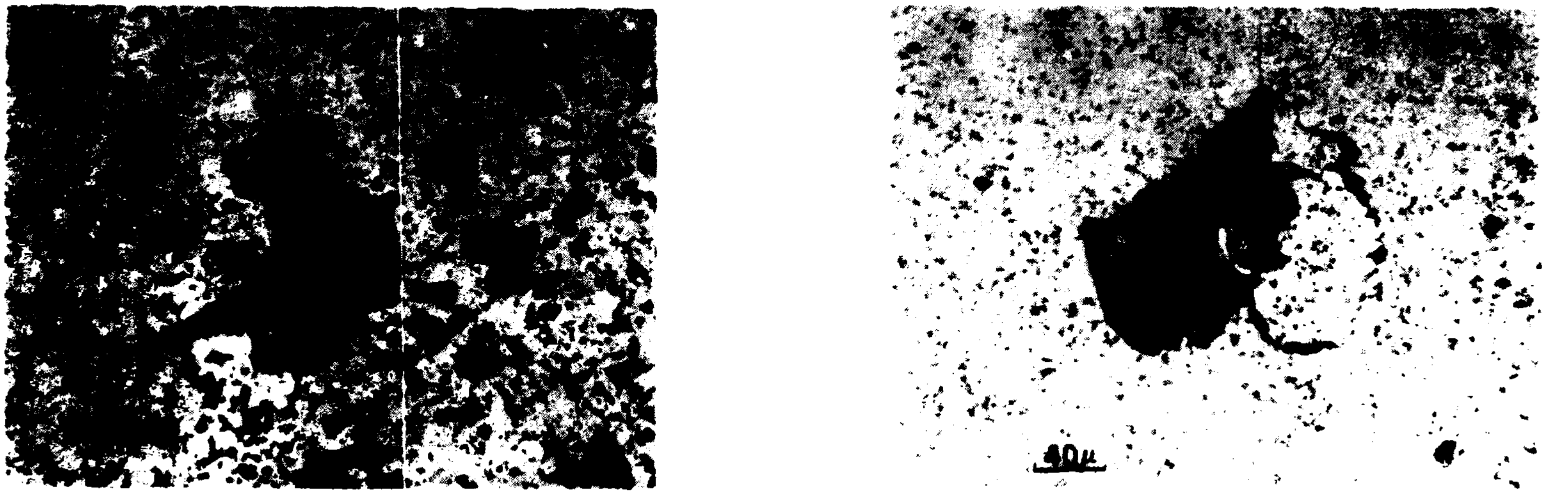

c) KBI Reaction Bonded Si_3N_4. Particle Velocity = 79 mps

d) NC 350 Reaction Bonded Si_3N_4. Particle Velocity = 79 mps

Figure 5. Typical Impacts with 300 Micron SiC Particles

GTE 3502 Pressureless Sintered Si_3N_4

a) intergranular radial crack

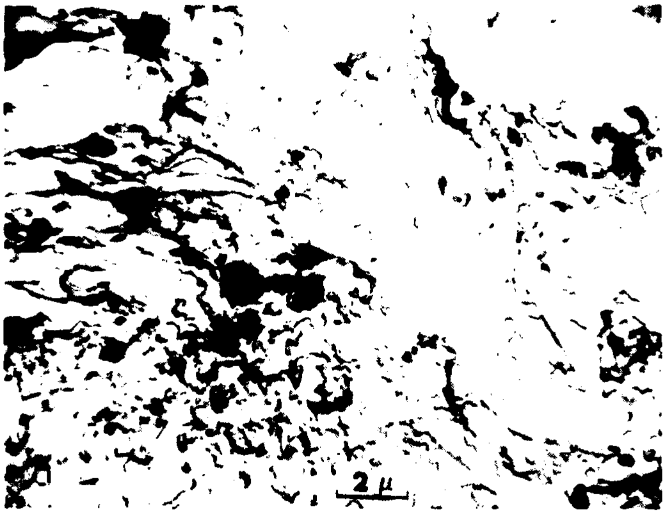

GTE 3502 Pressureless Sintered Si_3N_4

b) plastic flow in impact crater

Figure 6. Details of Damage from SiC Particle Impact (102 Micron Particle, 52 mps Velocity)

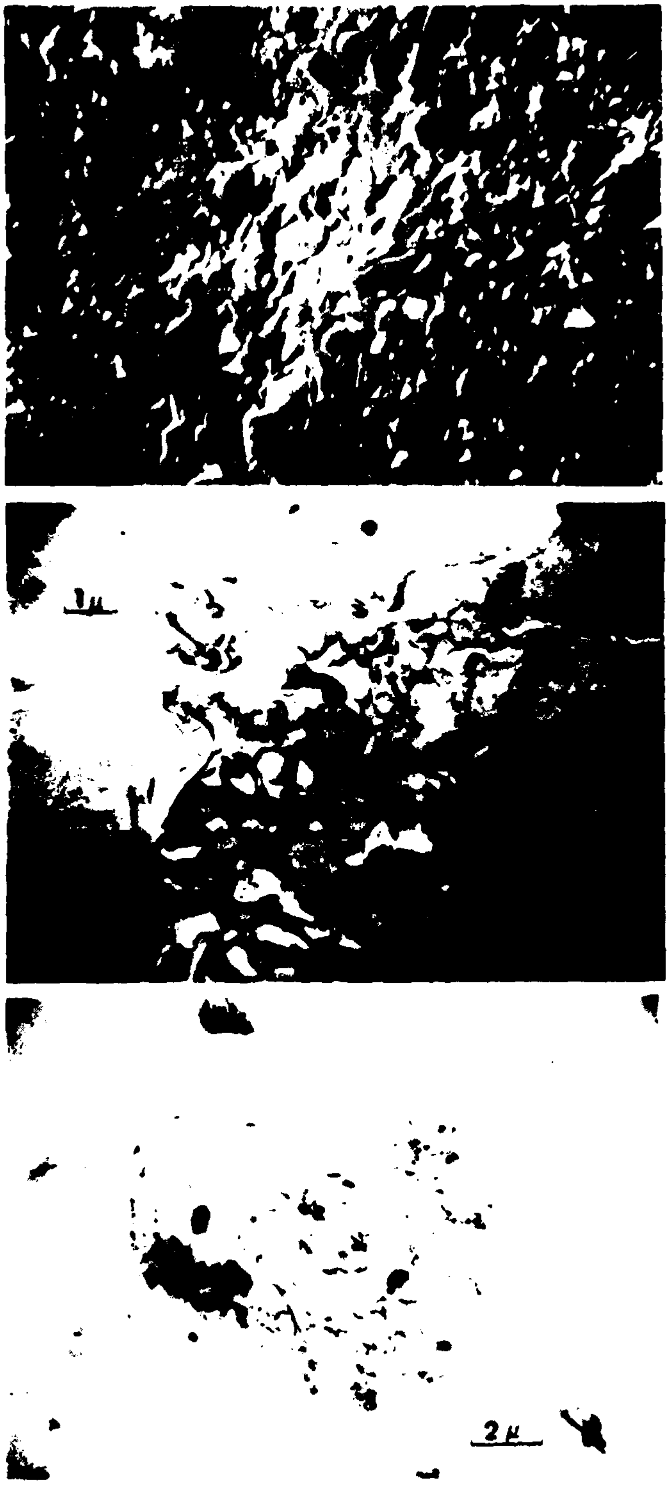

A. NC132 Hot Pressed Si_3N_4

Particle size = 115 microns

Particle velocity = 219 mps

B. GTE 3502 Pressureless Sintered Si_3N_4

Particle size = 49 microns

Particle velocity = 241 mps

C. NC 350 Reaction Bonded Si_3N_4

Particle size = 273 microns

Particle velocity = 188 mps

Figure 7. Typical Impact Damage Produced by Quartz Particles

2.1.5 Summary

All four Si_3N_4 targets impacted with SiC particles exhibited elastic-plastic impact which is characterized by a highly deformed impact crater and radial and lateral cracks propagating from the impact area. Erosion weight loss per impact was proportional to the fourth power of particle radius. The exponential velocity dependence varied apparently randomly between three and four. Erosion weight loss for the two forms of reaction bonded Si_3N_4 was the same and approximately one order of magnitude greater than hot-pressed and pressureless sintered Si_3N_4 under the same particle size/velocity test conditions. Weight loss on the hot-pressed and pressureless sintered targets was also indistinguishable.

Damage produced by quartz particles did not conform to characteristic elastic-plastic impact damage. Damage on hot-pressed and pressureless sintered Si_3N_4 was characterized by shallow intergranular chipping and no secondary crack formation, and both the radius and velocity exponents for erosion dependence were lower than for erosion with SiC particles. Erosion weight loss beween the two targets was again indistinguishable. The reaction bonded silicon nitrides did exhibit some secondary cracking on impact with quartz, but the nature of the cracking was circumferential rather than radial or lateral.

The type of damage produced during erosion of the Si_3N_4 targets was more a function of particle type or relative target/particle properties than of variation in particle size or velocity. Models for elastic-plastic impact relate erosion to a function of target hardness and fracture toughness. The correlation of erosion weight loss with the models is discussed in the next section. It will be shown that for elastic-plastic impact, the microstructural variation, such as grain size and amount of second phase including porosity, of these tagets is sufficiently accounted for in the fracture toughness and hardness values and does not have to be incorporated specifically in a model to explain or predict elastic-plastic erosion behavior. Microstructural variation may be a significant variable below the elastic-plastic threshold (Si_3N_4 impacted with quartz particles) because impact damage in this regime is primarily intergranular or inter-pore.

2.2 PHASE II - CORRELATION OF EXPERIMENTAL EROSION DATA WITH ELASTIC-PLASTIC IMPACT MODELS

2.2.1 Introduction

Recent investigations have shown that a number of erosion mechanisms for ceramics can exist and that erosion and impact is a complex process (Refs. 1, 2, 3 and 4). Essentially, two types of models have been proposed for solid particle impact (single particle) and erosion (multi particle) of brittle materials. The earlier models were based on elastic interaction between target and particle and predicted that material removal occurs by the intersection of ring cracks on the target surface. This process has been observed on several materials under static and low velocity impact conditions with relatively large spherical particles (Refs. 3 and 4). More recent analysis has treated static and dynamic plastic indentation, which is characterized by plastic deformation of the contact area between the particle and the target, with radial cracks propagating outward on planes nearly parallel to the surface. This type of damage, termed elastic-plastic, is observed for impact with angular particles of generally greater hardness than the target (Refs. 1 and 2).

Two expressions have been derived for elastic-plastic impact (Refs. 6 and 7). Details of the derivations are given in the references. Generally, the expressions relate erosion to the depth of damage and area of lateral cracking. The expressions are as follows:

$$V \propto \frac{(\rho_p \rho_t \mu_p \mu_t)^{2/3}}{(\sqrt{\rho_p \mu_p} + \sqrt{\rho_t \mu_t})^{8/3}} \qquad {\rho_p}^{19/12} {R_p}^{11/13} {v_p}^{19/6} {K_c}^{-4/3} H^{-1/4} \qquad (1)$$

after Evans (Ref. 6)

$$V \propto \frac{(\rho_p \rho_t \mu_p \mu_t)^{2/3}}{(\sqrt{\rho_p \mu_p} + \sqrt{\rho_t \mu_t})^{8/3}} \qquad {\rho_p}^{11/19} {R_p}^{11/3} {v_p}^{22/9} {K_c}^{-4/3} H^{1/9} \qquad (2)$$

after Ruff and Weiderhorm (Ref. 7)

where V = erosion volume loss per impact
ρ_p = particle density
ρ_t = target density
μ_p = particle shear modulus
μ_t = target shear modulus
R_p = particle radius
v_p = particle velocity
K_c = target fracture toughness
H = target hardness

The major differences between the two expressions are in the particle density, particle velocity and target hardness dependencies. These expressions are based on single impacts and were developed for isotropic materials under idealized conditions. The validity of the above expressions to predict erosion can be assessed by comparing a plot of experimental erosion data as a function of the expressions.

2.2.2 Results

Five target materials were eroded with SiC and quartz particles. The targets were NC132 hot-pressed Si_3N_4, GTE 3502 pressureless sintered Si_3N_4, NC350 reaction bonded Si_3N_4, KBI reaction bonded Si_3N_4 and Intran I MgF_2. Properties relevant to erosion are shown in Table 5. Particle properties are also given.

Table 5

Target and Particle Properties

	Shear Modulus* (GPa)	Fracture Toughness (MPam$^{1/2}$)	Hardness (GPa)	Microstructure
Hot-pressed Si_3N_4 NC 132	131	5	16	~2μ grain size-fully dense. Minor grain boundary phase
Pressureless-sintered Si_3N_4 GTE 3502	105	6	12	~2μ grainsize-98% dense. Significant grain boundary phase.
Reaction-sintered Si_3N_4 NC 350	70	2.2	7.5	75% dense-porosity 0.5-7μ. Multi-phase grain boundary phase.
Reaction-sintered Si_3N_4 KBI	60	2.2	5	75% dense-porosity 2-50μ. Multi-phase-60μ Si grains.
Hot-pressed MgF_2 Irtran 1	48	1	6	Fully dense-single phase. ~2μ grain size.
SiC	172	0.7	23	
Quartz	39	3	6	

* Shear modulus calculated from the expression $G = E/2(1+\gamma)$ where E = elastic modulus and γ is Poisson's ratio assumed to be 0.22 for all materials.

Six particle sizes between 10 and 385 microns average quartz particles and 8 and 940 microns average SiC particles were used for erosion testing. Between three and five particle velocities for each particle size were evaluated. All tests were performed at 90-degree impingement and ambient temperature. Erosion test data is given in Appendix B.

All of the targets impacted with SiC particles exhibited elastic-plastic impact. MgF_2 impacted with quartz particles also exhibited elastic-plastic impact. The other targets impacted with quartz exhibited very little if any damage outside of the particle-target contact area and for hot-pressed and pressureless sintered silicon nitride, damage was characterized by shallow intergranular chipping.

The validity of the expressions for elastic-plastic impact can be assessed by plotting erosion weight loss normalized by the appropriate particle size and velocity dependence versus the functions of particle and target particles predicted by the models. These plots are shown in Figures 8 and 9. The data points are average values of all data for a single target calculated on a logarithmic basis. The error bars correspond to ± one standard deviation also calculatd on a logarithmic basis. A line with a slope of one is drawn through the data points for those targets which exhibited elastic-plastic erosion damage. In both cases, the actual slope through the data points is 1.25 and 1.5 for Figures 8 and 9, respectively. The data for targets which did not exhibit elastic-plastic impact when impacted with quartz particles

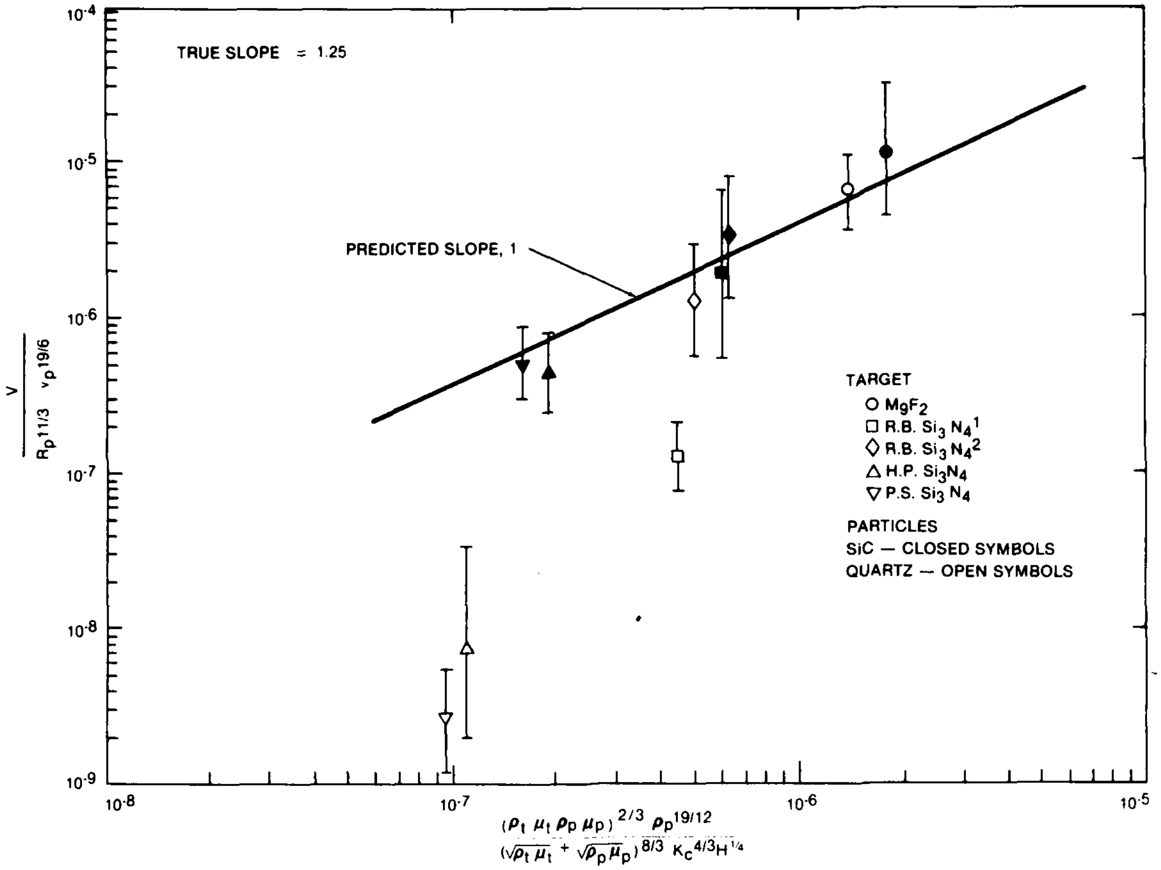

Figure 8. Erosion as a Function of Target and Particle Properties from Equation (1)

(hot-pressed, pressureless sintered and NC350 reaction bonded Si_3N_4) are in the correct order as predicted by both relationships, but fall well below the data line for elastic-plastic impact. The most remarkable result is that the experimental erosion data fit both models equally well although there are two major differences in the expressions; the dependence on particle velocity and target hardness. The power function of velocity from expression (1) is 3.17 which approximates the experimental value. The power function of velocity in expression (2) is lower at 2.44 and is also lower than observed experimentally in this work for elastic-plastic impact conditions. A lower velocity exponent has been observed in other work (Weiderhorn, private communication). The hardness exponents are (-1/4) for expression (1) and (+1/9) for expression (2). Although the targets exhibit a wide range of hardnesses, the small hardness dependence is not sufficient to separate the two expressions.

These results indicate that further experimental work is necessary before the model which most accurately describes elastic-plastic erosion can be ascertained, and that both models provide a reasonable fit with the experimental

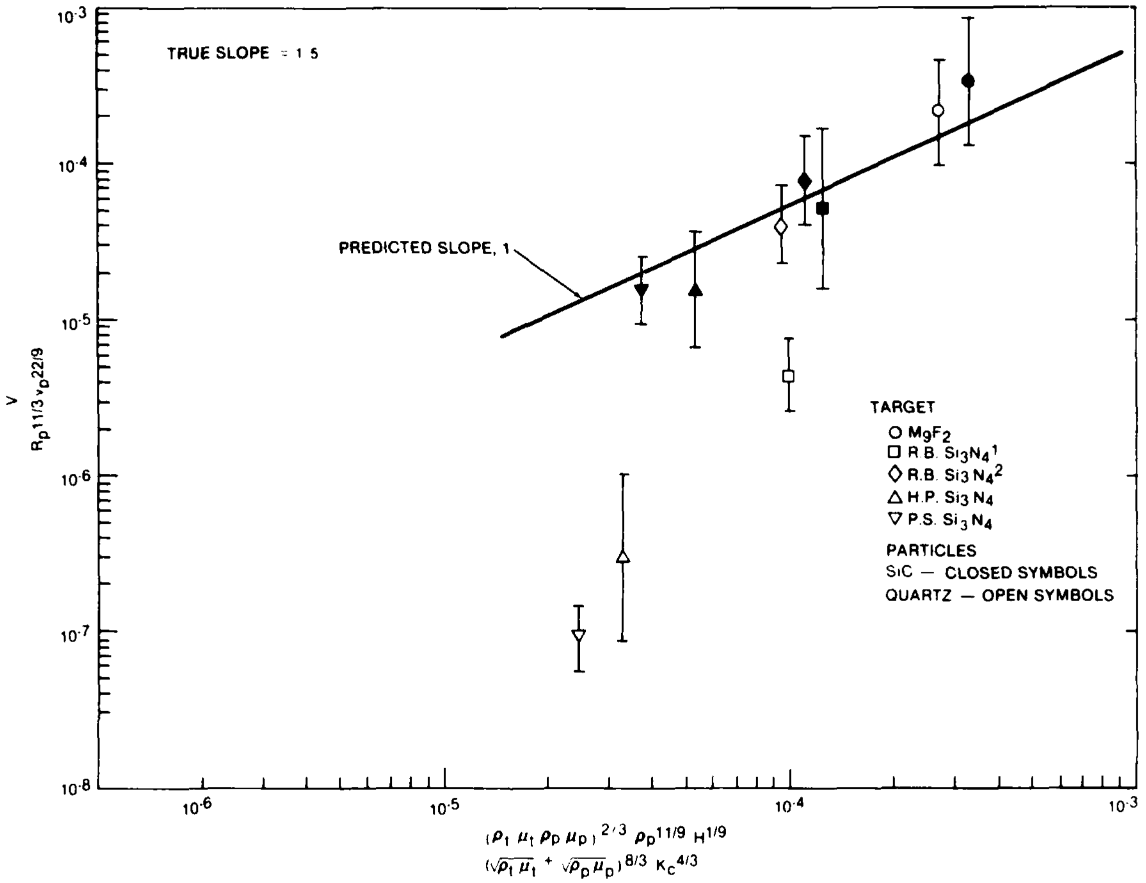

Figure 9. Erosion as a Function of Target and Particle Properties from Equation (2)

erosion data. The results further suggest that for the targets investigated, microstructural variation such as grain size and amount and type of second phase are sufficiently accounted for in the fracture toughness and hardness values and do no need to be considered separately in the models.

2.3 PHASE III - EFFECT OF NUMBER OF IMPACTS ON EROSION IN THE ELASTIC-PLASTIC RESPONSE REGIME

Models have recently been proposed to characterize the damage which occurs on impact with a relatively hard, angular projectile on a softer target surface. This damage system has been termed elastic-plastic and is characteristic of many situations in a dust erosion environment in the subsonic velocity regime. The laterally cracked material is responsible for most of the erosion loss. The models, which are based on single impact damage, predict that erosion is proportional to a function of particle size, velocity and density; and target fracture toughness and hardness. The usefulness of the models for explaining and predicting actual erosion behavior is dependent in part on the effect of number of impacts on material loss. It is known that for rain erosion and for solid particle erosion occurring by elastic interaction, that an incubation period exists prior to the onset of uniform erosion (Refs. 3 and 4).

A MgF_2 target was subjected to impact conditions from single particle to 10^{10} impacts which simulated a natural dust environment (quartz sand) in the subsonic velocity regime. Six narrow particle size ranges varying between 10 and 385 microns average diameter and up to five velocities for each particle size were used for the investigation. For this target-particle system, erosion weight loss follows the function of particle size and velocity ($R^{3.7}V^{3.2}$) predicted by the elastic-plastic model (Ref. 6) and the single impact damage is characteristic of elastic-plastic impact. Three series of tests were performed to assess the effect of number of impacts on erosion. These can be conveniently separated into the following: weight loss changes as a function of number of impacting particles, effect of starting surface finish on erosion weight loss, and examination and measurement of single and second impacts on the damage area of the initial impact.

There was no consistent effect of number of impacts on erosion weight loss between 10^2 and 10^{10} total particle impacts. On a plot showing erosion normalized by $R^{3.7}V^{3.2}$ (the function of particle size and velocity predicted by the model) versus number of impacts, the data points fall in a one order of magnitude band. It was also shown, again on a weight loss basis that the amount of material removed by the first impact is not significantly different from that removed by the 50th impact on the same area.

The effect of starting surface finish on erosion was assessed by comparing results between a polished starting surface and a heavily pre-damaged surface. Initially, more material was lost from the pre-damaged surface than from the polished surface. However, this initial effect was not maintained and for heavy erosion conditions, the total weight loss was the same for both starting surface conditions. The results indicate that starting surface finish is not a significant variable for conditions of heavy erosion.

Examination and measurement of single impact damage revealed that for a given particle size-velocity condition the volume of material removed per impact varied over three orders of magnitude. This large variation is due primarily to differences in particle orientation during impact which results from the irregular angular natural quartz particles. The large variation precludes determination of significant differences between initial and second impacts using standard statistical procedures. However, a comparison between arithmetic means and standard deviations calculated from common logarithms of the measured volume removed indicate there is not a significant difference between the amount of material removed by the first impact and that removed by subsequent impacts on the initial impact damage area. The average values for volume loss by second impacts are within the one standard deviation range for volume loss by the initial impacts.

The results of this investigation indicate that there is not a significant incubation or damage enhancement effect for conditions which simulate a dust erosion environment in the subsonic velocity regime when the damage is characterized by elastic-plastic impact. The results further indicate that the model developed for elastic-plastic impact, which was based on single impacts, is applicable to heavy erosion conditions.

This phase of the program is discussed in detail in Technical Report No. 7 and in the "Effect of Number of Impacts on Erosion of Polycrystalline MgF_2 in the Elastic-Plastic Response Regime" Journal of the American Ceramic Society, Vol. 63, No. 3-4, March-April, 1980, pp. 121-126.

2.4 PHASE IV - EROSION OF A TWO-PHASE TARGET - ALSIMAG 614 Al_2O_3

Alsimag 614 Al_2O_3, a common radome material, was eroded with quartz particles to simulate a dust erosion environment. Three particle size ranges of quartz (1-30, 75-149 and 203-297 microns) accelerated to velocities between 30 and 313 m/sec were used for erosion tests. The target is sintered Al_2O_3 containing approximately four percent glass which resides at the grain boundaries. The Al_2O_3 grain size averages about 10 microns and the glassy phase can be as wide as 4 microns at grain boundary triple points. Erosion of this target did not exhibit a consistent velocity dependence for the three particle sizes. Erosion was proportional to particle radius cubed over the entire range of particle sizes, but the velocity exponent varied between three for the smaller particles and one for the larger particles at higher velocities. This variation can be related to the two-phase nature of the microstructure.

Examination of the eroded surfaces revealed that damage from 10 micron particle impacts was characterized by flow of the glassy grain boundary phase and minimal damage to the Al_2O_3 grains. Erosion occurs by flow and removal of the glass to the extent that entire Al_2O_3 grains are lost. An example of a surface heavily eroded by 10 micron quartz particles is shown in Figure 10A. The depth of erosion corresponds to approximately four grain diameters. As can be seen, little damage is sustained by the Al_2O_3 grains. As the particle size was increased, chipping of the Al_2O_3 grains occurred in addition to flow of the glass. An example is shown in Figure 10B. This chipping is similar to that which occurs on hot-pressed Si_3N_4 impacted with quartz particles.

A more extensive discussion on this subject can be found in Technical Report No. 4 and in "Solid Particle Erosion of High Technology Ceramics (Si_3N_4, Glass-Bonded Al_2O_3 and MgF_2)", ASTM STP 664, Erosion: Prevention and Useful Applications, pp. 101-122, 1979.

2.5 PHASE V - EFFECT OF EROSION ON STRENGTH

Strength in three-point bending after erosion with quartz particles was determined for NC132 hot-pressed Si_3N_4, NC350 reaction bonded Si_3N_4 and Alsimag 614 glass bonded Al_2O_3. Particle sizes ranging from 10 to 385 microns and particle velocities between 15 and 315 mps were used for the erosion

A. 10μ Particle size

285 m/sec Velocity

Contact radius ~2μ

Depth of erosion ~50μ

$E \propto R^3V^3$

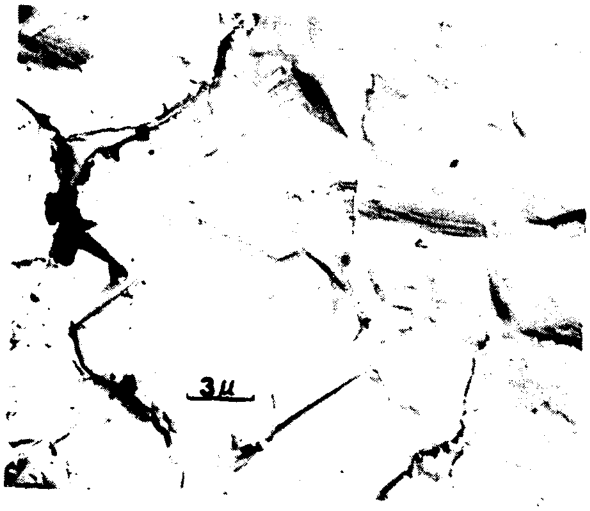

B. 250μ Particle size

46 m/sec Velocity

Contact radius ~13μ

Depth of erosion ~6μ

$E \propto R^3V$

Figure 10. Glass Bonded Al_2O_3 Impacted with Quartz

tests. The strength results are given in Table 6. The baseline strengths (prior to erosion) plus and minus one standard deviation are given for each target material. An estimate of the critical flaw size is also given. This was calculated from fracture toughness values using the relationship for three-point bend specimens (Ref. 8). The strengths after erosion are shown as a function of the baseline strengths by giving the percentages which have strengths greater than +1, and less than -1 standard deviation of the non-eroded material strength.

Hot-pressed Si_3N_4 and the GB Al_2O_3 did not exhibit a strength decrease under these test conditions for erosion depths up to 31 μm. For hot-pressed Si_3N_4 this depth corresponds to 3×10^8 particle impacts or 600 grams of dust on a 0.71 cm^2 area. There was a trend toward strength increase (fracture stress for 50 percent of the specimens was greater than one standard deviation above the baseline strength), which indicates that a "polishing" phenomenon may be occurring. No specimens failed at a stress lower than the one standard deviation band. The erosion depth is approximately three times the estimated critical flaw size, which indicates that under these test conditions the effective flaw size produced by erosion is no larger than pre-existing flaws characteristic of the "standard" machined surface. (Because large numbers of flaws are introduced by erosion or machining, the effective stress concentration will depend on both size and spacing of flaws. In contrast, critical flaw sizes were calculated for isolated flaws.) In confirmation, examination of the eroded surfaces in cross section did not reveal apparent subsurface damage; that is, the structure under the eroded area was indistinguishable from that below the as-machined surface and subsurface cracking was not apparent.

Table 6

Strength Distribution of Eroded Specimens
Relative to Standard Strength

	Pre-Erosion Baseline				Post-Erosion Strength Distribution (%)		
	$\sigma_F \pm 1$ Standard Deviation (MPa)	Critical Flaw Size (μm)	Number of Tests	Maximum Erosion Depth (μ)	Above +1 Standard Deviation	Within ± 1 Standard Deviation	Less Than -1 Standard Deviation
Hot-pressed Si_3N_4	798 ± 128	11	25	31	50	50	0
Glass-bonded Al_2O_3	252 ± 21	43	51	35	41	43	16
Reaction-bonded Si_3N_4	278 ± 10	17	17	360	6	12	82*

* Minimum strength = 81 MPa corresponding to critical flaw size of ≈200 μm.

The trend toward a strength increase is not as conclusive with GB Al_2O_3 as with hot-pressed Si_3N_4 since 16 percent of the specimens failed at stresses below the one standard deviation range. Furthermore, although the maximum depth of erosion (approx. 35 μm) is approximately four grain diameters, this also corresponds to the estimated critical flaw size of the baseline material. However, the results indicate that erosion under these test conditions does not produce flaws greater than those inherent to the assintered surface. There was no significant variation in strength with erosion test conditions (particle size and velocity) for either hot-pressed Si_3N_4 or GB Al_2O_3.

Reaction bonded Si_3N_4 did exhibit a marked strength decrease under these erosion test conditions. Strength decreased rapidly for the first 100 μm erosion depth and remained essentially constant at 100 MPa up to the maximum depth tested (350 μm). The lowest strength (81 MPa) corresponds to an increase in estimated critical flaw size over the baseline material of one order of magnitude (17 μm compared with 200 μm). The depth of subsurface cracks perpendicular to the surface is also approximately 200 μm for this erosion condition.

According to the model for elastic-plastic impact response, the strength of the target (σ_F) should be dominated by radial crack formation by the following relation (1)

$$\sigma_F \propto \frac{K_c^{1.4}}{V^{0.5}R^{0.8}}$$

where K_c = target fracture toughness,
V = particle velocity, and
R = particle radius.

A log-log plot of strength versus ($V^{0.5}R^{0.8}$) for reaction bonded Si_3N_4 does result in a line with slope = 1 for erosion with particle sizes of 115, 273 and 385 microns.

Since quartz is the most erosive constituent of natural dusts and the particle size-velocity conditions are typical of airborne dust, these results have direct practical significance and indicate that a strength decrease does not necessarily occur for erosion conditions, which produce appreciable material removal (hot-pressed Si_3N_4 and Alsimag 614 glass bonded Al_2O_3). This would be expected to apply as long as the load-bearing volume is not reduced significantly.

A more detailed discussion of this subject is given in Technical Report Nos. 5 and 6, and "Solid Particle Erosion of High Technology Ceramics (Si_3N_4, Glass-Bonded Al_2O_3 and MgF_2)", ASTM STP 664, Erosion: Prevention and Useful Applications, pp. 101-122, 1979.

2.6 PHASE VI - STATIC FATIGUE OF CERAMICS

Variable strain rate and deadweight load tests were conducted on four ceramics in various aqueous solutions at temperatures to 900°C. The ceramics were single crystal Al_2O_3, A1995 Al_2O_3, NC132 hot-pressed Si_3N_4 and NC350 reaction reaction bonded Si_3N_4. Most of the work was performed on the last two materials.

Hot-pressed Si_3N_4 did exhibit time-dependent failure and strength decreased with increase in available moisture. Fractures were intergranular. It is thought that the stress corrosion of the glassy grain boundary phase inherent in this material is responsible for the strength decrease. Reaction bonded Si_3N_4 in the as-fired condition also exhibited time-dependent strength reduction as a function of increasing moisture content. However, no decrease was observed when the oxide surface layer was removed prior to testing.

A model was proposed for the mechanism of stress corrosion of hot-pressed Si_3N_4 based on ion exchange occurring in the glassy grain boundary phase.

Further discussion on this subject is given in Technical Reports 1, 2 and 3 and in "Stress Corrosion of Silicon Nitride", Jr. Am. Cer. Soc., Vol. 59, No. 9-10, pp. 391-396, 1976.

REFERENCES

1. Evans, A.G., Gulden, M.E. and Rosenblatt, M., Proc. Roy. Soc., Lond. A. 361 (1978) 343.

2. Gulden, M.E., " "Solid Particle Erosion of High Technology Ceramics", ASTM STP 664 - Erosion: Prevention and Useful Applications.

3. Adler, W.F. and Sha, G.T., "Analytical Modeling of Subsonic Particle Erosion", Report AFML-TR-72-144, WPAFB, Ohio (1972).

4. Oh, H.L., Oh, K.O.L., Vaidyanathan, S. and Finnie, I., "On the Shaping of Brittle Solids by Erosion and Ultrasonic Cutting", NBS Special Publication 348 (1972) 119.

5. Adler, W.F. and Hooker, S.V., "Characterization of Transparent Materials for Erosion Resistance", Report AFML-TR-76-16, WPAFB, Ohio (1976).

6. Evans, A.G., in Treatise on Materials Science and Technology, Vol. 16, Erosion, C.M. Preece Ed., Academic Press, NY (1979), P1.

7. Ruff, A.W. and Wiederhorn, S.M., ibid, p. 69.

8. Evans, A.G., in Fracture Mechanics of Ceramics 1, R.C. Bradt, D.P.H. Hasselman and F.F. Lange, Eds., Plenum Press, NY (1974), p. 17.

APPENDIX A

EROSION TEST FACILITY

APPENDIX A

EROSION TEST FACILITY

TEST RIG

Erosion testing is performed with a stationary target impacted by particles accelerated in an air stream. Particles are injected into the air stream 3.05 metres from the target to provide sufficient distance for acceleration. High pressure, filtered and chemically dried air is used for the particle carrier gas. Particles are injected into the gas stream using either a precision, high-pressure, Plasmadyne powder feeder (for long-time tests of $>10^6$ particle impacts) or a smaller powder feeder which uses a weighted charge of particles. Moat tests were performed using the smaller feeder.

Particle flow is regulated so that particle-particle interaction in the air stream and at the specimen surface can be considered negligible. This flow rate corresponds to ~1 gram per minute.

Exit air velocity is determined with a pitot tube connected to a mercury manometer to monitor total pressure (P_T) and to a water manometer to monitor static pressure (P_S). The pitot tube is placed 1.27 cm from the nozzle exit which corresponds to the target position. The following relationship is used to calculate air velocity:

$$\frac{V}{\sqrt{T}} = \sqrt{2g.J.C_p \left[1 - \left(\frac{P_S}{P_T}\right)^{\frac{\gamma - 1}{\gamma}}\right]}$$

where V is velocity, T is the discharge temperature, g is the acceleration due to gravity, J is the mechanical equivalent of heat, C_p is the specific heat of the gas at constant pressure, and γ is the ratio of specific heats of the gas at constant pressure and constant volume. Current barometric pressure is used for the calculation, and the solution is computerized.

Maximum exit air velocity can be varied continuously between 15 and 343 (sonic velocity) m/sec at room temperature. The velocity variation across the 0.95 cm diameter nozzle is less than 5 percent.

In addition to exit gas velocity, the gas velocity where the particles enter the air stream is also determined by measuring static pressure and use of conventional Fanno line functions.

Target specimen size is greater than the nozzles to ensure that all particles impact the target.

PARTICLE VELOCITY

Considerable effort at Solar has been devoted to analyzing the acceleration characteristics of dust particles introduced into a high-velocity fluid. A general aerodynamic solution was developed assuming the particles react as Stokesian spheres in an accelerating gas stream. The derivation is given in pages 31 through 43.

The accuracy of this solution was determined by comparing the predicted particle velocities with measured particle velocities using the rotating double disc technique (Ruff, A.W. and Ives, L.R., Wear, 35 [1975] p. 195.)

The results are shown in Figure A-1 for quartz particles of various sizes and velocities. As can be seen, there is good agreement between the two methods of determining particle velocity. In view of the good correlation between measured and calculated particle velocities and the time-consuming process required to measure particle velocities, the calculated values were used for most of this work.

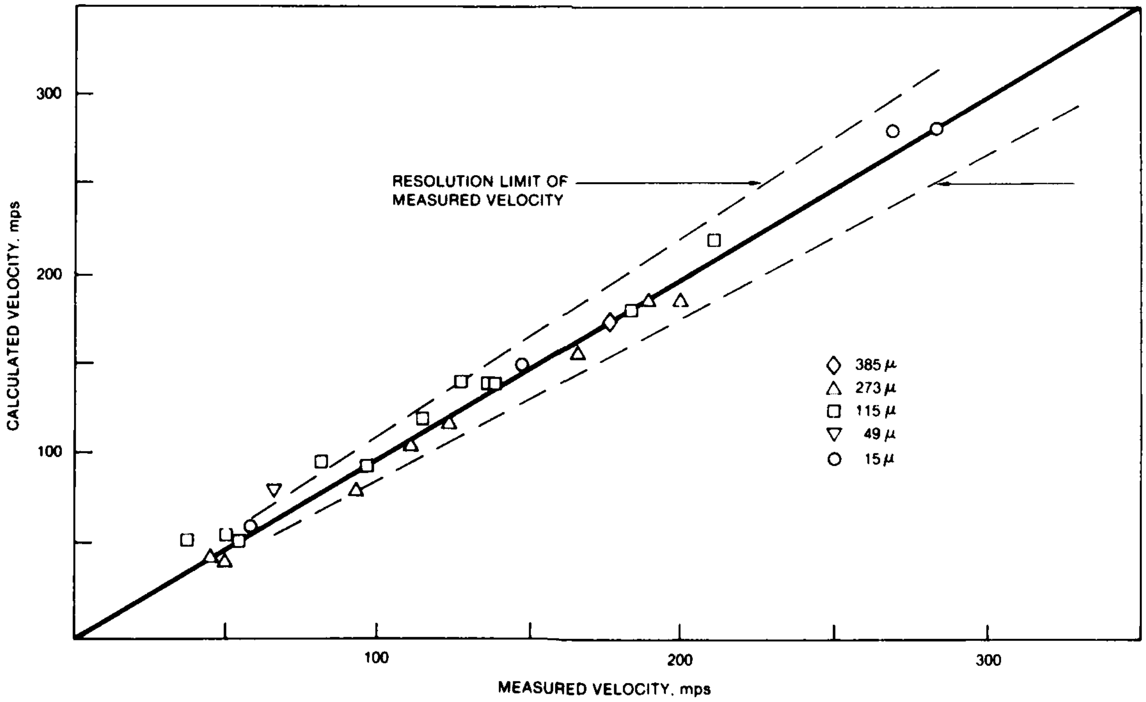

Figure A-1. Comparison of Quartz Particle Velocity Calculated from Aerodynamic Considerations and Measured by Rotating Double Disc Technique

FLOW PARAMETERS FOR PARTICULATE CLOUDS

A measure of the drag and inertia of a particle is the "range" or "carry". This is the distance the particle will travel in the direction of its initial velocity when projected into a motionless viscous fluid. The time to travel this distance is theoretically infinite, but the "range" concept is useful as a criterion for the threshold size for particle damage to surfaces. For example, if the range is less than the boundary layer thickness, then the particle will never reach the surface. Also, the range concept will give a measure (it is simply related to the inertia parameter discussed elsewhere) of the departure of the particle trajectories from the fluid streamlines in the vicinity of a solid body. The larger the range, the more the trajectories will depart from the streamlines in curving flow.

For spherical particles in the Stokesian motion regime ($Re \ll 1.0$), the drag coefficient $C_D = 24/Re$, where the particle Reynolds number, $Re = V D_p/\nu$,

and ν = kinematic viscosity - ft^2/sec

V = velocity - fps

D_p = diameter of particle - ft

The equation of motion of the particle in the direction of the initial velocity, assuming that the fluid drag is the only force acting in this direction, is:

$$m \frac{dV}{dt} = -C_D \frac{1}{2} \rho V^2 A \qquad \text{with } V = V_o \text{ when } t = 0,$$

i.e.,

$$\rho_p \frac{\pi D_p^3}{6} \frac{dV}{dt} = -\frac{24\nu}{V D_p} \frac{1}{2} \rho V^2 \frac{\pi D_p^2}{4}$$

or

$$\frac{dV}{dt} = -\frac{18\mu V}{\rho_p D_p^2} \qquad (1)$$

where m = mass of particle - slugs

ρ_p = density of particle - $slugs/ft^3$

A = projected area of particle - ft^2

ρ = density of fluid - $slugs/ft^3$

μ = absolute viscosity of fluid = $\rho\nu$ slug/ft sec

Solutions of this equation are

$$V = V_o e^{-\frac{18\mu}{\rho_p D_p^2} t} = V_o e^{-\frac{t}{\tau}} \tag{2}$$

$$S = V_o \tau (1 - e^{-\frac{t}{\tau}}) = S_o (1 - e^{-\frac{t}{\tau}}) \tag{3}$$

where $\tau = \rho_p D_p^2 / 18\mu$ is a time constant related to $S_o = V_o \tau$, the "range" or "carry".

It is apparent that τ is the time for the velocity to drop to 36.8 percent of its initial value V_o when the distance travelled will be 63.2 percent of S_o.

The range S_o can also be thought of as the distance that the particle would travel in time τ if its initial velocity V_o were maintained. Plots of velocity and distance against time make these points clear.

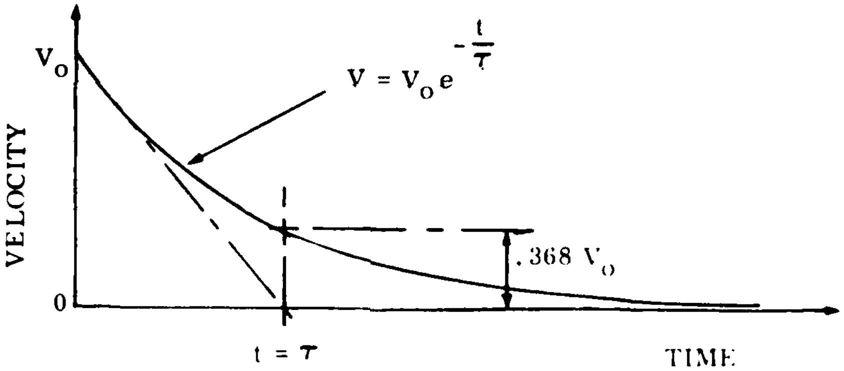

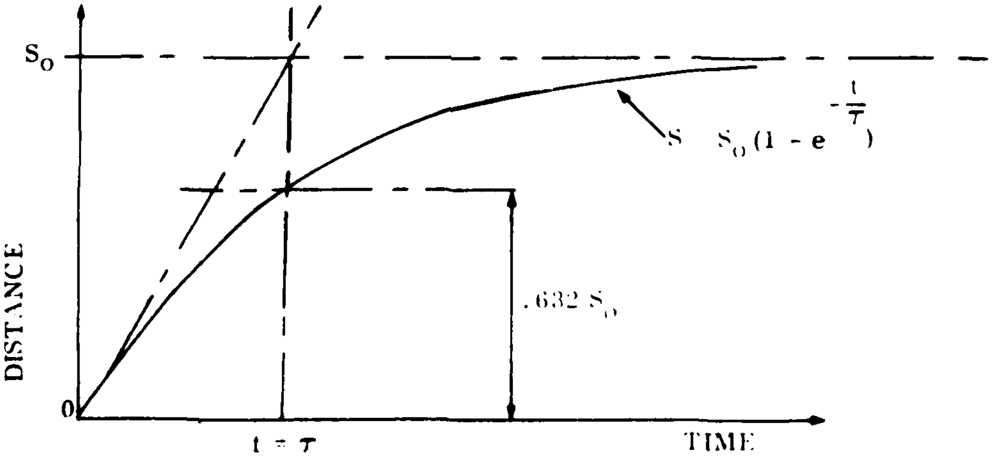

For flow in the vicinity of a solid body, the trajectories of the particles will be determined by the ratio of the range to a characteristic length of the body. For a sphere or cylinder in crossflow, this length has (traditionally) been taken as the radius, giving rise to the so-called inertia parameter $K = 2S_0/D$

$$K = \frac{\rho_p D_p^2 V_o}{9\mu D} \tag{4}$$

The inertia parameter is clearly dimensionless, and the trajectories of all particles with the same value K will be geometrically similar so long as the particle can be regarded as a massive point (i.e., its dimensions are small compared to the impacting body) and its presence does not interfere with the flow pattern (i.e., the concentration is sufficiently small).

For flow of particles in a fluid falling under the influence of gravity, the particles will accelerate until the drag plus bouyancy forces just balance the gravitational force. The terminal (or settling) velocity so reached is given when

$$\frac{1}{2}\rho V_t^2 C_D A + mg\left(\frac{\rho}{\rho_p}\right) = mg \tag{5}$$

where m = mass of the particle - slugs

ρ_p = density of the particle - slugs/ft^3

ρ = density of fluid - slugs/ft^3

A = drag area of particle - ft^2

C_D = drag coefficient

V_t = terminal velocity - fps

g = gravitational acceleration - ft/sec^2

For a spherical particle in the Stokesian regime, this becomes

$$\frac{1}{2}\rho V_t^2 \frac{24}{Re} \frac{\pi D_p^2}{4} \quad \frac{\pi D_p^3}{6} (\rho_p - \rho) g$$

or

$$V_t = \frac{gD_p^2}{18\mu}(\rho_p - \rho)$$

$$= \frac{gD_p^2\rho_p}{18\mu}\left(1 - \frac{\rho}{\rho_p}\right) \tag{6}$$

Substituting from (5) into (6), we get

$$V_t = \frac{gKD}{2V_o}\left(1 - \frac{\rho}{\rho_p}\right)$$

or

$$\frac{V_t V_o}{g D} = \frac{K}{2}\left(1 - \frac{\rho}{\rho_p}\right) \tag{7}$$

The quantity V_tV_o/gD is called the separation number and is also dimensionless like the inertia parameter K. If the density of the particles is large compared to the density of the propelling fluid, then the separation number = 1/2 the inertia parameter. The separation number is related to a body with characteristic dimension D and is a measure of the separation (or collection) efficiency of that body when impacted by a particulate cloud.

DYNAMICS OF PARTICULATE CLOUDS

Equation of Motion - A particle moving through a fluid with instantaneous velocity $\vec{V}$ will experience a resisting force given by

$$\begin{aligned} \vec{F} &= -\frac{1}{2}\rho(\vec{V} - \vec{U})^2 C_D A \hat{K} \\ &= -\frac{1}{2}\rho(\vec{W})^2 C_D A \hat{K} \end{aligned} \tag{8}$$

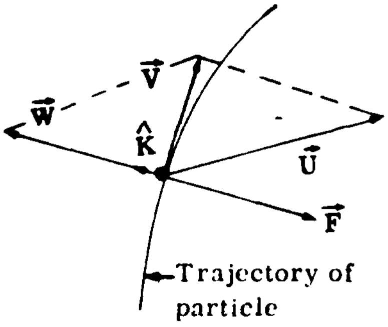

where $\vec{U}$ = local velocity of the fluid

$\vec{W}$ = velocity of the particle relative to the fluid = $\vec{V} - \vec{U}$

ρ = density of the fluid

C_D = drag coefficient of the particle

A = relevant projected area of the particle for the given drag coefficient

$\hat{K}$ = unit vector in the direction of relative motion

Neglecting all other body forces (including gravity), the equation of motion of the particle will be

$$m \frac{d\vec{V}}{dt} = \vec{F} = -\frac{1}{2} \rho (\vec{W})^2 C_D A \hat{K} \tag{9}$$

where m = mass of the particle

or

$$\frac{d}{dt} (\vec{U} + \vec{W}) = -\frac{C_D A \rho}{2m} (\vec{W})^2 \hat{K} \tag{10}$$

SPHERICAL PARTICLE IN UNIFORM VELOCITY FIELD

If the particle is spherical of diameter D_p and density ρ_p, then

$$m = \rho_p \frac{D_p{}^3}{6} \pi \tag{11}$$

and a good approximation to the drag coefficient is

$$C_D = .4 + \frac{24}{Re} \tag{12}$$

with $A = \frac{\pi D^2}{4}$ the projected frontal area

Also,

$$Re = \frac{|\vec{W}| D_p \rho}{\mu} \tag{13}$$

where μ = absolute viscosity of the fluid

If additionally, $\vec{V}$ is in the same direction as $\vec{U}$, then $-\vec{W}$ is also in this same direction, and with $\vec{U} = -U\hat{K}$, $\vec{V} = -V\hat{K}$, and $\vec{W} = W\hat{K}$, we get the scalar equations

$$W = U - V$$

and

$$\frac{d}{dt}(-U + W) = -\frac{1}{2}\frac{6}{\pi \rho_p D_p^3}(.4 + \frac{24\mu}{W D_p \rho})\rho \frac{\pi D^2}{4} W^2$$

$$= -\frac{.3\rho}{\rho_p D_p} W^2 + \frac{18\mu}{\rho_p D_p^2} W) \qquad (14)$$

The factor $18\mu/\rho_p D_p^2 = 1/\tau$ where τ is the Stokesian time constant associated with the range when $U = 0$. Also, if U is a constant velocity (i.e., a uniform fluid velocity field), then

$$\frac{d}{dt}(-U + W) = \frac{dW}{dt}$$

Putting

$$\frac{.3\rho}{\rho_p D_p} = \frac{1}{\delta}, \text{ we get}$$

$$\frac{dW}{dt} = -\frac{1}{\tau}(W + \frac{\tau}{\delta} W^2) \qquad (15)$$

which is the differential equation for the relative velocity W.

The solution of this equation is

$$\frac{t}{\tau} = \text{const} - \log(\frac{W}{1 + \frac{\tau}{\delta} W})$$

If

$$W = W_o \text{ when } t = 0,$$

then

$$\text{const} = \log\left[\frac{W_o}{1 + \frac{\tau}{\delta} W_o}\right]$$

and

$$t = \tau \log\left[\frac{W_o}{W}\,\frac{1 + \frac{\tau}{\delta} W}{1 + \frac{\tau}{\delta} W_o}\right] \qquad (16)$$

giving the time to reach a relative velocity W from an initial relative velocity W_o. It will be noted that the time for W to become zero is infinitely large. Also, when $t = \tau$ we have

$$\epsilon = \frac{W_o}{W}\left[\frac{1 + \frac{\tau}{\delta} W}{1 + \frac{\tau}{\delta} W_o}\right]$$

or

$$W = \frac{W_o}{\epsilon}\left\{1 + \frac{\tau}{\delta} W_o \left(1 - \frac{1}{\epsilon}\right)\right\}^{-1}$$

$$= .368\, W_o \left\{1 + .632 \frac{\tau}{\delta} W_o\right\}^{-1} \qquad (17)$$

This shows the influence of the stronger drag coefficient as compared to the Stokesian solution. For Stokesian flow, τ is the time for the relative velocity to drop to 36.8 percent of the initial value, whereas with the stronger drag forces the relative velocity drops to somewhat less than 36.8 percent in time τ, depending on the value of $(\tau/\delta) W_o$. Also, for $1/\delta = 0$ or $W_o \rightarrow 0$, the Stokesian equations are regained.

Now equation (15) may be rewritten as

$$W \frac{dW}{dS_{rel}} = -\frac{1}{\tau}\left(W + \frac{\tau}{\delta} W^2\right)$$

or

$$\frac{dW}{dS_{rel}} = -\frac{1}{\tau}\left(1 + \frac{\tau}{\delta} W\right) \qquad (18)$$

where S_{rel} is the distance that the particle travels relative to the fluid.

The solution to equation (18) is

$$\frac{S_{rel}}{\tau} = \text{constant} - \frac{\delta}{\tau} \log\left(1 + \frac{\tau}{\delta} W\right)$$

when

$$S_{rel} = 0 \qquad W = W_o \qquad \text{const} = \frac{\delta}{\tau}\left(1 + \frac{\tau}{\delta} W_o\right)$$

Then,

$$S_{rel} = \delta \log \left(\frac{1 + \frac{\tau}{\delta} W_o}{1 + \frac{\tau}{\delta} W} \right) \tag{19}$$

The distance the particle will travel in time t is given by

$$S = \int V \, dt = \int (U - W) \, dt$$

So

$$S = Ut - \int W \, dt$$

$$= Ut - S_{rel} \tag{20}$$

Substituting for t from equation (16) and S_{rel} from equation (19) gives

$$S = U\tau \log \left[\frac{W_o}{W} \, \frac{1 + \frac{\tau}{\delta} W}{1 + \frac{\tau}{\delta} W_o} \right] - \delta \log \left[\frac{1 + \frac{\tau}{\delta} W_o}{1 + \frac{\tau}{\delta} W} \right]$$

$$= U \tau \log \left[\frac{W_o}{W} \left(\frac{1 + \frac{\tau}{\delta} W}{1 + \frac{\tau}{\delta} W_o} \right)^{1 + \frac{\delta}{U\tau}} \right] \tag{21}$$

and this is the distance travelled by the particle to attain a relative velocity W from an initial relative velocity W_o in a uniform fluid velocity field of value U.

If the particle is introduced into the stream with initial velocity zero, then the initial relative velocity $W_o = U$ and the instantaneous relative velocity $W = U - V$. Equation (21) becomes

$$S = U \tau \log \left[\left(\frac{U}{U - V} \right) \left(\frac{1 + \frac{\tau}{\delta} (U - V)}{1 + \frac{\tau}{\delta} U} \right)^{1 + \frac{\delta}{U\tau}} \right]$$

or putting

$$\lambda = \frac{V}{U} ,$$

$$S = U\tau \log \left[\left(\frac{1}{1 - \lambda} \right) \left(\frac{1 + \frac{\tau U}{\delta} (1 - \lambda)}{1 + \frac{\tau U}{\delta}} \right)^{1 + \frac{\delta}{U\tau}} \right] \tag{22}$$

Similarly, equation (16) for the time becomes

$$t = \tau \log \left[\left(\frac{1}{1 - \lambda} \right) \frac{1 + \frac{\tau U}{\delta} (1 - \lambda)}{1 + \frac{\tau U}{\delta}} \right] \tag{23}$$

Now $\tau U/\delta = \rho D_p U/60\mu = Re_o/60$, where Re_o is the Reynolds number for the particle based on fluid velocity U. Also writing $U\tau = S_o$ - the "range" for Stokesian motion, equations (22) and (23) may be written

$$\frac{S}{S_o} = \log\left(\frac{1}{1 - \lambda}\right) + \left(1 + \frac{60}{Re_o}\right) \log \left[1 - \frac{\lambda}{1 + \frac{60}{Re_o}} \right] \tag{24}$$

and

$$\frac{t}{\tau} = \log\left(\frac{1}{1 - \lambda}\right) + \log \left[1 - \frac{\lambda}{1 + \frac{60}{Re_o}} \right] \tag{25}$$

For pure Stokesian motion, these equations reduce to the limiting equations as $Re_o \longrightarrow 0$

$$\frac{S}{S_o} = \log\left(\frac{1}{1 - \lambda}\right) - \lambda \tag{26}$$

and

$$\frac{t}{\tau} = \log\left(\frac{1}{1 - \lambda}\right) \tag{27}$$

All four above equations are dimensionless and will therefore be valid for any spherical particle in any viscous fluid. The parameters Re_o, S_o and τ will, however, depend on the properties of the particular fluid and particle considered. It should be noted that

$$S_o = U\tau = U D_p^2 \rho_p/18\mu = \left[\frac{D_p \rho_p}{18 \rho}\right] Re_o \tag{28}$$

SPHERICAL PARTICLE IN ACCELERATING VELOCITY FIELD

The following equation relates final particle velocity, V, as accelerated by a gas flow of uniform velocity, U, over a section, S, where the particle velocity at the entrance of the section, Vo, is not necessarily zero.

$$\frac{S}{S_o} = \log \left[\left(\frac{1 - \frac{V_o}{U}}{1 - \frac{V}{U}} \right) \left(\frac{1 + \frac{R_{eo}}{60} \left(1 - \frac{V}{U}\right)}{1 + \frac{R_{eo}}{60} \left(1 - \frac{V_o}{U}\right)} \right) \right] \qquad 29$$

$$+ \frac{60}{R_{eo}} \, \mathrm{Log} \left[\frac{\left[1 + \frac{R_{eo}}{60} \left(1 - \frac{V}{U}\right)\right]}{\left[1 + \frac{R_{eo}}{60} \left(1 - \frac{V_o}{U}\right)\right]} \right]$$

This form is readily derivable from equation 21 given that:

$$W_o = U - V_o$$

$$W = U - V$$

$$\frac{\delta}{U\tau} = \frac{60}{R_{eo}}$$

and

$$U\tau = S_o$$

The above equation can now be used to iteratively calculate final particle velocity at the exit of a gas stream where gas velocity varies with position in the stream. The iteration approximates the following explicit expression for particle velocity at tube exit V_f:

$$V_f = \int_0^L V \left(R_{eo} (L)\right) \cdot dL$$

i.e., an accelerating velocity field can be mathematically considered in small segments to estimate the integral of particle acceleration over its length. Variability of Reynolds number with tube length can be considered in this manner.

"Basic" language computer codes shown in Figures A-2a and A-2b have been written to compute particle velocity in an accelerating gas stream by the above method.

In the form shown in Figure A-2b, it estimates gas velocity and density as linear functions of tube length from tube entrance and entrance conditions. The form in Figure A-2a accepts a nonlinear gas velocity and density versus length input.

```
1000 [illegible] "THE S[illegible] [illegible] FOR [illegible]"
1010 PRINT
1020 [illegible] TUBE INCREMENT SIZE[illegible]
1030 INPUT S1
1032 IF [illegible] 5 THEN 1034
1033 [illegible]
1034 [illegible]=0.05
1035 [illegible]
1036 [illegible]=0.[illegible]
1040 PRINT "TUBE INCREMENT SIZE[illegible]"FT"
1050 DISP "AIR VISCOSITY, LB HR-F[illegible]"
1060 INPUT 0
1070 PRINT "AIR VISCOSITY=";0;"LB HR-LB"
1080 DISP "PARTICLE DIAMETER, MICRONS"
1090 INPUT I
1100 PRINT "PARTICLE DIAMETER=";I;"MICRONS"
1110 DISP "PARTICLE DENSITY,GM/CC"
1120 INPUT A[illegible]
1130 PRINT "PARTICLE DENSITY=";A[illegible];"GM/CC"
1140 [illegible]0=0
1150 [illegible]=0
1160 [illegible]=0
1170 [illegible]=
1180 [illegible] PARTICLE VEL[illegible]=[illegible]"FPS"
1190 [illegible] THEN 1510
1200 PR[illegible]
1210 [illegible]RENT AIR DENSIT[illegible]LB FT[illegible]
1220 INPUT A[illegible]
1230 PR[illegible]"CURRENT AIR DENSITY=[illegible]LB FT↑3"
1240 [illegible] CURRENT AIR VELOCITY[illegible]
1250 INPUT [illegible]
1260 [illegible]RRENT AIR [illegible]FPS
1270 [illegible]
1280 [illegible]
1290 [illegible]
1300 [illegible] MICRONS [illegible]
1310 [illegible]
1320 [illegible]
1330 [illegible] CON[illegible]
1340 [illegible]
1350 [illegible]
1360 [illegible]
1370 [illegible]
1380 [illegible] 1400
1390 [illegible]
1400 [illegible]=
1410 [illegible]
1420 [illegible]
1430 [illegible] THEN 14[illegible]
1440 [illegible]
1450 [illegible]
1460 [illegible]
1470 [illegible]
1480 [illegible] THEN 15[illegible]
1490 [illegible] THE[illegible]
1500 [illegible] FT.
1510 [illegible]
1520 [illegible]
1530 [illegible]
1540 [illegible]
1550 [illegible]
```

Figure A-2a. Computer Code for Calculating Exit Particle Velocity From Accelerating Tube With Variable Gas Velocity

```
1000 PRINT TAB15"CALCULATION OF V 30 FOR U0 0
1010 A7=0
1020 PRINT
1030 DISP "TUBE INCREMENT SIZE, FT";
1040 INPUT S1
1050 IF S1 5 THEN 1070
1060 GOTO 1090
1070 =0.05
1080 GOTO 1110
1090 =0.01
1100 IF A7=1 THEN 1420
1110 PRINT "TUBE INCREMENT SIZE = ";S1;"FT"
1120 IF A7=1 THEN 1420
1130 DISP "AIR VISCOSITY, LB HR-FT";
1140 INPUT U
1150 PRINT "AIR VISCOSITY=";U;" LB HR-LB
1160 DISP "PARTICLE DIAMETER, MICRONS";
1170 INPUT D
1180 PRINT "PARTICLE DIAMETER= ";D;"MICRONS"
1190 DISP "PARTICLE DENSITY,GM CC";
1200 INPUT A2
1210 PRINT "PARTICLE DENSITY= ";A2;"GM/CC"
1220 V0=0
1230 V=V0
1240 N=0
1241 DISP "INITIAL AIR VELOCITY,FPS";
1242 INPUT U0
1243 PRINT "INITIAL AIR VELOCITY= ";U0;"FPS"
1244 DISP "FINAL AIR VELOCITY";
1245 INPUT U2
1246 PRINT "FINAL AIR VELOCITY";U2;"FPS"
1247 DISP "INITIAL AIR DENSITY";
1248 INPUT A0
1249 PRINT "INITIAL AIR DENSITY";A0;" LB/FT↑3
1250 V0=V
1260 PRINT "CURRENT PARTICLE VELOCITY =";V;"FPS"
1270 IF N 9.9999 THEN 1670
1280 PRINT
1290 U=U0+(U2-U0) 10*(N+S1/2)
1300 A1=A0*U0/U
1350 N=N+S1
1360 R=A1*U*D 0*3600*3.94E-05 12
1370 GOTO 1390
1380 PRINT "REYNOLDS NUMBER=";R
1390 T=1.142E-07*A2*D↑2/U
1400 GOTO 1420
1410 PRINT "TIME CONSTANT=";T
1420 S0=U*T
1430 S=S1
1440 =0.2*U
1450 V=V+(1+ - S1-S))
1460 GOTO 1480
1470 V=V+(1+.*(S1-S)
1480 L=V U
1490 IF L 1 THEN 1510
1500 GOTO 1550
1510 DISP "TUBE INCREMENT IS TOO LONG
1520 WAIT 3000
1530 A7=1
1540 GOTO 1030
1550 L0=V0 U
1560 S=S0*(LOG (1-L0) (1-L))+(1+60 R *LOG  1+R 60*(1-L) (1+R 60*(1-L0) ) )
1570 IF S S1 THEN 1600
1580 DISP S
1590 GOTO 1610
1600 DISP "               ";S
1610 IF S 1.0001*S1 THEN 1450
1620 IF S .9999*S1 THEN 1640
1630 IF S S1 THEN 1470
1640 PRINT "INCREMENT OF PART. TRAV.=";S;"FT."
1650 PRINT N;" INCREMENTS"
1660 IF N 10.01 THEN 1250
1670 DISP "DONE
1680 REWIND
1690 END
```

Figure A-2b. Computer Code for Calculating Exit Particle Velocity From Accelerating Tube With Assumed Linear Variable Gas Velocity and Density Over Length

APPENDIX B

EROSION TEST RESULTS

APPENDIX B

EROSION TEST RESULTS

The erosion data used to generate Figures 8 and 9 is given. Volume loss per impact is the average value of as many as ten tests. Number of impacts were calculated assuming spherical particles of the diameter given. All erosion tests were performed at 90-degree impingement angle and ambient temperature.

NC 132 Hot -Pressed Si_3N_4/SiC Particles

Part. Dia. (μm)	Velocity (mps)	$\frac{\text{Volume Loss}}{\text{Impact (m}^3\text{)}}$	$R^{3.67}V^{3.17}$	$\frac{\text{Volume Loss}}{R^{3.67}V^{3.17}}$	$R^{3.67}V^{2.44}$	$\frac{\text{Volume Loss}}{R^{3.67}V^{2.44}}$
8	61	1.1×10^{-21}	7.1×10^{-15}	1.5×10^{-7}	3.5×10^{-16}	3.1×10^{-6}
	122	1.5×10^{-20}	6.4×10^{-14}	2.3×10^{-7}	1.9×10^{-15}	7.9×10^{-6}
	183	5.9×10^{-20}	2.3×10^{-13}	2.6×10^{-7}	5.1×10^{-15}	1.2×10^{-5}
	244	1.6×10^{-19}	5.7×10^{-13}	2.8×10^{-7}	1.0×10^{-14}	1.6×10^{-5}
	292	3.4×10^{-19}	1.0×10^{-12}	3.4×10^{-7}	1.6×10^{-14}	2.1×10^{-5}
50	58	1.4×10^{-18}	5.0×10^{-12}	2.8×10^{-7}	2.6×10^{-13}	5.4×10^{-6}
	107	1.5×10^{-17}	3.5×10^{-11}	4.3×10^{-7}	1.15×10^{-12}	1.3×10^{-5}
	153	3.7×10^{-17}	1.1×10^{-10}	3.4×10^{-7}	2.8×10^{-12}	1.3×10^{-5}
	198	8.1×10^{-17}	2.5×10^{-10}	3.2×10^{-7}	5.2×10^{-12}	1.6×10^{-5}
	241	1.5×10^{-16}	4.6×10^{-10}	3.3×10^{-7}	8.4×10^{-12}	1.8×10^{-5}
102	52	2.0×10^{-17}	4.9×10^{-11}	4.1×10^{-7}	2.7×10^{-12}	7.4×10^{-6}
	97	1.3×10^{-16}	3.5×10^{-10}	3.7×10^{-7}	1.25×10^{-11}	1.0×10^{-5}
	138	3.4×10^{-16}	1.1×10^{-9}	3.1×10^{-7}	2.9×10^{-11}	1.2×10^{-5}
	178	7.2×10^{-16}	2.4×10^{-9}	3.0×10^{-7}	5.25×10^{-11}	1.4×10^{-5}
	217	1.4×10^{-15}	4.5×10^{-9}	3.1×10^{-7}	8.9×10^{-11}	1.6×10^{-5}
305	79	2.25×10^{-15}	1.0×10^{-8}	2.25×10^{-7}	4.2×10^{-10}	5.35×10^{-6}
	113	1.9×10^{-14}	3.2×10^{-8}	5.9×10^{-7}	1.0×10^{-9}	1.9×10^{-5}
	145	4.4×10^{-14}	7.0×10^{-8}	6.3×10^{-7}	1.8×10^{-9}	2.4×10^{-5}
	176	9.1×10^{-14}	1.3×10^{-7}	7.0×10^{-7}	2.95×10^{-9}	3.1×10^{-5}
560	69	2.6×10^{-14}	6.2×10^{-8}	4.2×10^{-7}	2.8×10^{-9}	9.3×10^{-6}
	98	1.65×10^{-13}	1.9×10^{-7}	8.8×10^{-7}	6.6×10^{-9}	2.5×10^{-5}
	126	1.1×10^{-12}	4.2×10^{-7}	8.1×10^{-7}	1.2×10^{-8}	9.2×10^{-5}
	152	2.3×10^{-12}	7.5×10^{-7}	9.6×10^{-7}	1.9×10^{-8}	1.2×10^{-4}
940	31	7.2×10^{-15}	3.3×10^{-8}	2.2×10^{-7}	2.7×10^{-9}	2.7×10^{-6}
	59	3.4×10^{-13}	2.5×10^{-7}	1.4×10^{-6}	1.3×10^{-8}	2.6×10^{-5}
	85	9.7×10^{-13}	8.0×10^{-7}	1.2×10^{-6}	3.1×10^{-8}	3.1×10^{-5}
	109	1.7×10^{-12}	1.8×10^{-6}	9.7×10^{-7}	5.7×10^{-8}	3.0×10^{-5}
	132	3.4×10^{-12}	3.2×10^{-6}	1.0×10^{-6}	9.1×10^{-8}	3.7×10^{-5}

NC 132 Hot-Pressed Si_3N_4/Quartz Particles

Part. Dia. (μm)	Velocity (mps)	$\frac{\text{Volume Loss}}{\text{Impact } (m^3)}$	$R^{3.67}V^{3.17}$	$\frac{\text{Volume Loss}}{R^{3.67}V^{3.17}}$	$R^{3.67}V^{2.44}$	$\frac{\text{Volume Loss}}{R^{3.67}V^{2.44}}$
10	61	5.9×10^{-21}	1.6×10^{-14}	3.7×10^{-7}	8.0×10^{-16}	7.4×10^{-6}
	120	1.1×10^{-20}	1.4×10^{-13}	7.9×10^{-8}	4.1×10^{-15}	2.7×10^{-6}
	175	1.7×10^{-20}	4.5×10^{-13}	3.8×10^{-8}	1.0×10^{-14}	1.7×10^{-6}
	229	2.2×10^{-20}	1.1×10^{-12}	2.0×10^{-8}	2.0×10^{-14}	1.1×10^{-6}
	285	2.9×10^{-20}	2.1×10^{-12}	1.4×10^{-8}	3.4×10^{-14}	8.5×10^{-7}
49	109	3.9×10^{-19}	3.4×10^{-11}	1.15×10^{-8}	1.2×10^{-12}	3.25×10^{-7}
	157	5.3×10^{-19}	1.1×10^{-10}	9.8×10^{-9}	3.0×10^{-12}	1.8×10^{-7}
	202	6.6×10^{-19}	2.4×10^{-10}	2.75×10^{-9}	5.5×10^{-12}	1.2×10^{-7}
	247	8.4×10^{-19}	4.6×10^{-10}	1.8×10^{-9}	9.0×10^{-12}	9.3×10^{-8}
64	57	4.4×10^{-19}	1.2×10^{-11}	3.7×10^{-8}	6.1×10^{-13}	7.2×10^{-7}
	106	9.1×10^{-19}	8.4×10^{-11}	1.1×10^{-8}	2.8×10^{-12}	3.2×10^{-7}
	152	1.3×10^{-18}	2.6×10^{-10}	5.0×10^{-9}	6.7×10^{-12}	1.9×10^{-7}
	196	1.7×10^{-18}	5.9×10^{-10}	2.9×10^{-9}	1.25×10^{-11}	1.4×10^{-7}
	239	2.3×10^{-18}	1.1×10^{-9}	2.1×10^{-9}	2.0×10^{-11}	1.15×10^{-7}
115	52	2.0×10^{-18}	7.55×10^{-11}	2.6×10^{-8}	4.2×10^{-12}	4.8×10^{-7}
	93	6.3×10^{-18}	4.8×10^{-10}	1.3×10^{-8}	1.7×10^{-11}	3.7×10^{-7}
	140	1.1×10^{-17}	1.55×10^{-9}	7.1×10^{-9}	4.6×10^{-11}	2.4×10^{-7}
	180	1.3×10^{-17}	3.9×10^{-9}	3.3×10^{-9}	8.6×10^{-11}	1.5×10^{-7}
	219	1.2×10^{-17}	7.2×10^{-9}	1.7×10^{-9}	1.4×10^{-10}	8.6×10^{-8}
273	45	1.5×10^{-17}	1.1×10^{-9}	1.4×10^{-8}	7.1×10^{-11}	2.1×10^{-7}
	84	5.9×10^{-17}	8.2×10^{-9}	7.2×10^{-9}	3.2×10^{-10}	1.8×10^{-7}
	120	9.7×10^{-17}	2.55×10^{-8}	3.8×10^{-9}	7.7×10^{-10}	1.3×10^{-7}
	155	1.4×10^{-16}	5.8×10^{-8}	2.4×10^{-9}	1.4×10^{-9}	1.0×10^{-7}
	188	1.3×10^{-16}	1.1×10^{-7}	1.2×10^{-9}	2.3×10^{-9}	5.6×10^{-8}
385	175	4.7×10^{-16}	3.0×10^{-7}	1.6×10^{-9}	6.7×10^{-9}	7.0×10^{-8}

GTE Pressureless Sintered Si_3N_4/SiC Particles

Part. Dia. Size (μ)	Velocity (mps)	$\frac{\text{Volume Loss}}{\text{Impact } (m^3)}$	$R^{3.67}V^{3.17}$	$\frac{\text{Volume Loss*}}{R^{3.67}V^{3.17}}$	$R^{3.67}V^{2.44}$	$\frac{\text{Volume Loss}}{R^{3.67}V^{2.44}}$
8	61	3.8×10^{-21}	7.1×10^{-15}	5.35×10^{-7}	3.5×10^{-16}	1.1×10^{-5}
	183	5.3×10^{-20}	2.3×10^{-13}	2.3×10^{-7}	5.11×10^{-15}	1.0×10^{-5}
	292	2.9×10^{-19}	1.0×10^{-12}	2.9×10^{-7}	1.6×10^{-14}	1.8×10^{-5}
102	52	2.65×10^{-17}	4.8×10^{-11}	5.5×10^{-7}	2.7×10^{-12}	9.8×10^{-6}
	138	3.4×10^{-16}	1.1×10^{-9}	3.1×10^{-7}	2.9×10^{-11}	1.2×10^{-5}
	217	1.8×10^{-15}	4.5×10^{-9}	4.0×10^{-7}	8.9×10^{-11}	2.0×10^{-5}
305	42	5.3×10^{-16}	1.4×10^{-9}	3.8×10^{-7}	9.0×10^{-11}	5.9×10^{-6}
	113	1.7×10^{-14}	3.2×10^{-8}	5.3×10^{-7}	1.0×10^{-9}	1.7×10^{-5}
	176	6.6×10^{-14}	1.3×10^{-7}	5.1×10^{-7}	2.95×10^{-9}	2.2×10^{-5}
940	31	4.7×10^{-14}	3.3×10^{-8}	1.4×10^{-6}	2.7×10^{-9}	1.71×10^{-5}
	85	8.4×10^{-13}	8.0×10^{-7}	1.0×10^{-6}	3.1×10^{-8}	2.7×10^{-5}
	132	3.0×10^{-12}	3.2×10^{-6}	9.4×10^{-7}	9.14×10^{-8}	3.3×10^{-5}

GTE Pressureless Sintered Si_3N_4/Quartz Particles

Part. Dia. (μm)	Velocity (mps)	$\frac{\text{Volume Loss}}{\text{Impact (m}^3)}$	$R^{3.67}V^{3.17}$	$\frac{\text{Volume Loss}}{R^{3.67}V^{3.17}}$	$R^{3.67}V^{2.44}$	$\frac{\text{Volume Loss}}{R^{3.67}V^{2.44}}$
115	93	3.1×10^{-18}	4.8×10^{-10}	6.5×10^{-9}	1.7×10^{-11}	1.8×10^{-7}
	140	2.8×10^{-18}	1.55×10^{-9}	1.8×10^{-9}	4.6×10^{-11}	6.1×10^{-8}
	180	5.0×10^{-18}	3.9×10^{-9}	1.3×10^{-9}	8.6×10^{-11}	5.8×10^{-8}
	219	8.1×10^{-18}	7.2×10^{-9}	1.1×10^{-9}	1.4×10^{-10}	5.8×10^{-8}
273	45	1.4×10^{-17}	1.1×10^{-9}	1.3×10^{-8}	7.1×10^{-11}	2.0×10^{-7}
	84	4.7×10^{-17}	8.2×10^{-9}	5.7×10^{-9}	3.2×10^{-10}	1.5×10^{-7}
	120	1.2×10^{-16}	2.55×10^{-8}	4.7×10^{-9}	7.7×10^{-10}	1.6×10^{-7}
		8.4×10^{-17}		3.3×10^{-9}		1.1×10^{-7}
	155	9.7×10^{-17}	5.8×10^{-8}	1.7×10^{-9}	1.4×10^{-9}	6.9×10^{-8}
	188	1.7×10^{-16}	1.1×10^{-7}	1.5×10^{-9}	2.3×10^{-9}	7.4×10^{-8}
385	112	1.4×10^{-16}	7.2×10^{-8}	1.9×10^{-9}	2.3×10^{-9}	6.1×10^{-8}
	144	2.8×10^{-16}	1.6×10^{-7}	1.75×10^{-9}	4.2×10^{-9}	6.7×10^{-8}
	174	4.1×10^{-16}	3.0×10^{-7}	1.4×10^{-9}	6.7×10^{-9}	6.1×10^{-8}

NC 350 Reaction Sintered Si_3N_4/SiC Particles

Part. Dia. (μm)	Velocity (mps)	$\frac{\text{Volume Loss}}{\text{Impact (m}^3)}$	$R^{3.67}V^{3.17}$	$\frac{\text{Volume Loss}}{R^{3.67}V^{3.17}}$	$R^{3.67}V^{2.44}$	$\frac{\text{Volume Loss}}{R^{3.67}V^{2.44}}$
8	61	7.1×10^{-21}	7.1×10^{-15}	1.0×10^{-6}	3.5×10^{-16}	2.0×10^{-5}
	183	4.2×10^{-20}	2.3×10^{-13}	3.2×10^{-7}	5.1×10^{-15}	8.2×10^{-6}
	292	1.8×10^{-19}	1.0×10^{-12}	1.8×10^{-7}	1.6×10^{-14}	1.1×10^{-5}
102	52	2.2×10^{-16}	4.8×10^{-11}	4.6×10^{-6}	2.7×10^{-12}	8.15×10^{-5}
	138	2.3×10^{-15}	1.1×10^{-9}	2.1×10^{-6}	2.9×10^{-11}	7.9×10^{-5}
	217	1.1×10^{-14}	4.5×10^{-9}	2.4×10^{-6}	8.9×10^{-11}	1.2×10^{-4}
305	42	1.1×10^{-14}	1.4×10^{-9}	7.8×10^{-6}	9.0×10^{-11}	1.2×10^{-4}
	113	1.9×10^{-14}	3.2×10^{-8}	5.9×10^{-7}	1.0×10^{-9}	1.9×10^{-5}
	176	4.6×10^{-13}	1.3×10^{-7}	3.5×10^{-6}	2.95×10^{-9}	1.55×10^{-4}
940	31	5.8×10^{-14}	3.3×10^{-8}	1.8×10^{-6}	2.7×10^{-9}	2.15×10^{-5}
	85	5.4×10^{-12}	8.0×10^{-7}	6.75×10^{-6}	3.1×10^{-8}	1.7×10^{-4}
	132	2.2×10^{-11}	3.2×10^{-6}	6.9×10^{-6}	9.1×10^{-8}	2.4×10^{-4}

NC 350 Reaction Sintered Si_3N_4/Quartz Particles

Part. Dia. (μm)	Velocity (mps)	$\frac{\text{Volume Loss}}{\text{Impact } (m^3)}$	$R^{3.67}V^{3.17}$	$\frac{\text{Volume Loss}}{R^{3.67}V^{3.17}}$	$R^{3.67}V^{2.44}$	$\frac{\text{Volume Loss}}{R^{3.67}V^{2.44}}$
10	229	5.0×10^{-20}	1.1×10^{-12}	4.55×10^{-8}	2.0×10^{-14}	2.5×10^{-6}
	285	1.2×10^{-19}	2.1×10^{-12}	5.7×10^{-8}	3.4×10^{-14}	3.5×10^{-6}
49	109	2.6×10^{-18}	3.4×10^{-11}	7.6×10^{-8}	1.2×10^{-12}	2.2×10^{-6}
	157	1.5×10^{-17}	1.1×10^{-10}	1.4×10^{-7}	5.5×10^{-12}	2.7×10^{-6}
	202	2.9×10^{-17}	2.4×10^{-10}	1.2×10^{-7}	3.0×10^{-12}	9.7×10^{-6}
	247	5.4×10^{-17}	4.6×10^{-10}	1.2×10^{-7}	9.0×10^{-12}	6.0×10^{-6}
64	57	2.2×10^{-18}	1.2×10^{-11}	1.8×10^{-7}	6.1×10^{-13}	3.6×10^{-6}
	106	9.2×10^{-18}	8.4×10^{-11}	1.1×10^{-7}	2.8×10^{-12}	3.3×10^{-6}
	152	3.7×10^{-17}	2.6×10^{-10}	1.4×10^{-7}	6.7×10^{-12}	5.5×10^{-6}
	196	7.5×10^{-17}	5.9×10^{-10}	1.3×10^{-7}	1.25×10^{-11}	6.0×10^{-6}
	239	1.4×10^{-16}	1.1×10^{-9}	1.3×10^{-7}	2.0×10^{-11}	7.0×10^{-6}
115	93	1.2×10^{-16}	4.8×10^{-10}	2.5×10^{-7}	1.7×10^{-11}	7.1×10^{-6}
	140	3.0×10^{-16}	1.55×10^{-9}	1.9×10^{-7}	4.6×10^{-11}	6.5×10^{-6}
	180	7.9×10^{-16}	3.9×10^{-9}	2.0×10^{-7}	8.6×10^{-11}	9.2×10^{-6}
	219	1.2×10^{-15}	7.2×10^{-9}	1.7×10^{-7}	1.4×10^{-10}	8.6×10^{-6}
273	84	7.5×10^{-16}	8.2×10^{-9}	9.1×10^{-8}	3.2×10^{-10}	2.3×10^{-6}
	120	2.1×10^{-15}	2.55×10^{-8}	8.2×10^{-8}	7.7×10^{-10}	2.7×10^{-6}
	155	1.0×10^{-14}	5.8×10^{-8}	1.7×10^{-7}	1.4×10^{-9}	7.1×10^{-6}
	188	1.95×10^{-14}	1.1×10^{-7}	1.8×10^{-7}	2.3×10^{-9}	8.5×10^{-6}
385	78	1.6×10^{-15}	2.3×10^{-8}	7.0×10^{-8}	9.5×10^{-10}	1.7×10^{-6}
	112	6.2×10^{-15}	7.2×10^{-8}	8.6×10^{-8}	2.3×10^{-9}	2.7×10^{-6}
	144	2.1×10^{-14}	1.6×10^{-7}	1.3×10^{-74}	4.2×10^{-9}	5.0×10^{-6}
	174	1.5×19^{-13}	3.0×10^{-7}	5.0×10^{-7}	6.7×10^{-9}	2.2×10^{-6}

KBI Reaction Sintered Si_3N_4/SiC Particles

Part. Dia. (μm)	Velocity (mps)	$\frac{\text{Volume Loss}}{\text{Impact } (m^3)}$	$R^{3.67}V^{3.17}$	$\frac{\text{Volume Loss}}{R^{3.67}V^{3.17}}$	$R^{3.67}V^{2.44}$	$\frac{\text{Volume Loss}}{R^{3.67}V^{2.44}}$
8	61	7.1×10^{-21}	7.1×10^{-15}	1.0×10^{-6}	3.5×10^{-16}	2.0×10^{-5}
	183	1.3×10^{-19}	2.3×10^{-13}	3.1×10^{-5}	5.1×10^{-15}	2.5×10^{-5}
	292	6.7×10^{-19}	1.0×10^{-12}	6.7×10^{-7}	1.6×10^{-14}	4.2×10^{-5}
50	153	1.9×10^{-16}	1.1×10^{-10}	1.7×10^{-6}	2.8×10^{-12}	6.8×10^{-5}
	217	1.1×10^{-15}	3.3×10^{-10}	3.3×10^{-6}	6.5×10^{-12}	1.7×10^{-4}
102	52	1.9×10^{-16}	4.8×10^{-11}	4.0×10^{-6}	2.7×10^{-12}	7.0×10^{-5}
	138	3.6×10^{-15}	1.1×10^{-9}	3.3×10^{-6}	2.9×10^{-11}	1.2×10^{-4}
	217	1.4×10^{-14}	4.5×10^{-9}	3.1×10^{-6}	8.9×10^{-11}	1.6×10^{-4}
305	42	5.4×10^{-15}	1.4×10^{-9}	3.9×10^{-6}	9.0×10^{-11}	6.0×10^{-5}
	113	9.6×10^{-14}	3.2×10^{-8}	3.0×10^{-6}	1.0×10^{-9}	9.6×10^{-5}
	176	3.5×10^{-13}	1.3×10^{-7}	2.7×10^{-6}	2.95×10^{-9}	1.2×10^{-4}
940	31	2.9×10^{-13}	3.3×10^{-8}	8.8×10^{-6}	2.7×10^{-9}	1.1×10^{-4}
	85	3.1×10^{-12}	8.0×10^{-7}	3.9×10^{-6}	3.1×10^{-8}	1.0×10^{-4}
	132	9.2×10^{-12}	3.2×10^{-6}	2.9×10^{-6}	9.1×10^{-8}	1.0×10^{-4}

KBI Reaction Sintered Si_3N_4/Quartz Particles

Part. Dia. (μm)	Velocity (mps)	$\frac{\text{Volume Loss}}{\text{Impact } (m^3)}$	$R^{3.67}V^{3.17}$	$\frac{\text{Volume Loss}}{R^{3.67}V^{3.17}}$	$R^{3.67}V^{2.44}$	$\frac{\text{Volume Loss}}{R^{3.67}V^{2.44}}$
10	61	5.4×10^{-20}	1.6×10^{-14}	3.4×10^{-6}	8.0×10^{-16}	6.75×10^{-5}
	175	1.3×10^{-19}	4.5×10^{-13}	2.9×10^{-7}	1.0×10^{-14}	1.3×10^{-5}
	285	4.2×10^{-19}	2.1×10^{-12}	2.0×10^{-7}	3.4×10^{-14}	1.2×10^{-5}
115	52	1.8×10^{-16}	7.55×10^{-11}	2.4×10^{-6}	4.2×10^{-12}	4.3×10^{-5}
	93	5.4×10^{-16}	4.8×10^{-10}	1.1×10^{-6}	1.7×10^{-11}	3.2×10^{-5}
	139	2.4×10^{-15}	1.55×10^{-9}	1.55×10^{-6}	4.6×10^{-11}	5.2×10^{-5}
		1.2×10^{-15}	1.55×10^{-9}	7.7×10^{-7}	4.6×10^{-11}	2.6×10^{-5}
	180	3.8×10^{-15}	3.9×10^{-9}	9.7×10^{-7}	8.6×10^{-11}	4.4×10^{-5}
	219	7.5×10^{-15}	7.2×10^{-9}	1.0×10^{-6}	1.4×10^{-10}	5.4×10^{-5}
273	45	3.5×10^{-15}	1.1×10^{-9}	3.2×10^{-6}	7.1×10^{-11}	4.9×10^{-5}
	120	4.6×10^{-14}	2.55×10^{-8}	1.8×10^{-6}	7.7×10^{-10}	6.0×10^{-5}
	188	1.4×10^{-13}	1.1×10^{-7}	1.3×10^{-6}	2.3×10^{-9}	6.1×10^{-5}
385	41	6.5×10^{-15}	3.0×10^{-9}	2.2×10^{-6}	2.0×10^{-10}	3.25×10^{-5}
	112	1.8×10^{-13}	7.2×10^{-8}	2.5×10^{-6}	2.3×10^{-9}	7.8×10^{-5}
	174	5.4×10^{-13}	3.0×10^{-7}	1.8×10^{-6}	6.7×10^{-9}	8.1×10^{-5}

Irtran I Hot-Pressed MgF_2/Quartz Particles

Part. Dia. (μm)	Velocity (mps)	$\frac{\text{Volume Loss}}{\text{Impact } (m^3)}$	$R^{3.67}V^{3.17}$	$\frac{\text{Volume Loss}}{R^{3.67}V^{3.17}}$	$R^{3.67}V^{2.44}$	$\frac{\text{Volume Loss}}{R^{3.67}V^{2.44}}$
10	61	6.0×10^{-20}	1.6×10^{-14}	3.75×10^{-6}	8.0×10^{-16}	7.5×10^{-5}
	120	7.3×10^{-19}	1.4×10^{-13}	5.2×10^{-6}	4.1×10^{-15}	1.8×10^{-4}
	175	2.2×10^{-18}	4.5×10^{-13}	4.9×10^{-6}	1.0×10^{-14}	2.2×10^{-4}
	229	4.2×10^{-18}	1.1×10^{-12}	3.8×10^{-6}	2.0×10^{-14}	2.1×10^{-4}
	285	8.0×10^{-18}	2.1×10^{-12}	3.8×10^{-6}	3.4×10^{-14}	2.35×10^{-4}
49	58	9.4×10^{-18}	4.7×10^{-12}	2.0×10^{-6}	2.6×10^{-13}	3.6×10^{-5}
	109	2.2×10^{-16}	3.4×10^{-11}	6.5×10^{-6}	1.2×10^{-12}	1.8×10^{-4}
	157	4.7×10^{-16}	1.1×10^{-10}	4.3×10^{-6}	3.0×10^{-12}	1.6×10^{-4}
	202	1.6×10^{-15}	2.4×10^{-10}	6.7×10^{-6}	5.5×10^{-12}	2.9×10^{-4}
	247	2.5×10^{-15}	4.6×10^{-10}	5.6×10^{-6}	9.0×10^{-12}	2.8×10^{-4}
64	57	3.3×10^{-17}	1.2×10^{-11}	2.75×10^{-6}	6.1×10^{-13}	5.4×10^{-5}
	106	4.4×10^{-16}	8.4×10^{-11}	5.2×10^{-6}	2.8×10^{-12}	1.6×10^{-4}
	152	2.5×10^{-15}	2.6×10^{-10}	9.6×10^{-6}	6.7×10^{-12}	3.7×10^{-4}
	196	5.0×10^{-15}	5.9×10^{-10}	8.5×10^{-6}	1.25×10^{-11}	4.0×10^{-4}
	239	9.2×10^{-15}	1.1×10^{-9}	8.4×10^{-6}	2.0×10^{-11}	4.6×10^{-4}
115	52	6.6×10^{-16}	7.55×10^{-11}	8.7×10^{-6}	4.2×10^{-12}	1.6×10^{-4}
	93	3.7×10^{-15}	4.8×10^{-10}	7.7×10^{-6}	1.7×10^{-11}	2.2×10^{-4}
	139	1.5×10^{-14}	1.55×10^{-9}	9.7×10^{-6}	4.6×10^{-11}	3.3×10^{-4}
	180	3.7×10^{-14}	3.9×10^{-9}	9.5×10^{-6}	8.6×10^{-11}	4.3×10^{-4}
	219	6.0×10^{-14}	7.2×10^{-9}	8.3×10^{-6}	1.4×10^{-10}	4.3×10^{-4}
273	45	6.25×10^{-15}	1.1×10^{-9}	5.7×10^{-6}	7.1×10^{-11}	8.8×10^{-5}
	84	3.4×10^{-14}	8.2×10^{-9}	4.1×10^{-6}	3.2×10^{-10}	1.1×10^{-4}
	120	2.3×10^{-13}	2.55×10^{-8}	9.0×10^{-6}	7.7×10^{-10}	3.0×10^{-4}
	155	5.7×10^{-13}	5.8×10^{-8}	9.8×10^{-6}	1.4×10^{-9}	4.1×10^{-4}
	188	9.4×10^{-13}	1.1×10^{-7}	8.5×10^{-6}	2.3×10^{-9}	4.1×10^{-4}
385	41	6.2×10^{-15}	3.0×10^{-9}	2.1×10^{-6}	2.0×10^{-10}	3.1×10^{-5}
	78	2.3×10^{-13}	2.3×10^{-8}	1.0×10^{-5}	9.5×10^{-10}	2.4×10^{-4}
	112	1.7×10^{-12}	7.2×10^{-8}	2.4×10^{-5}	2.3×10^{-9}	7.4×10^{-4}
	144	2.0×10^{-12}	1.6×10^{-7}	1.25×10^{-5}	4.2×10^{-9}	4.8×10^{-4}
	174	3.6×10^{-12}	3.0×10^{-7}	1.2×10^{-5}	6.7×10^{-9}	5.4×10^{-4}

Irtran I Hot Pressed MgF_2/SiC Particles

Part. Dia. (μm)	Velocity (mps)	$\frac{\text{Volume Loss}}{\text{Impact (m}^3\text{)}}$	$R^{3.67}V^{3.17}$	$\frac{\text{Volume Loss}}{R^{3.67}V^{3.17}}$	$R^{3.67}V^{2.44}$	$\frac{\text{Volume Loss}}{R^{3.67}V^{2.44}}$
8	61	1.8×10^{-20}	7.0×10^{-15}	2.6×10^{-6}	3.5×10^{-16}	5.1×10^{-5}
	122	4.7×10^{-20}	6.4×10^{-14}	7.3×10^{-7}	1.9×10^{-15}	2.5×10^{-5}
	183	5.0×10^{-19}	2.3×10^{-13}	2.2×10^{-6}	5.1×10^{-15}	9.7×10^{-5}
	244	1.0×10^{-18}	5.7×10^{-13}	1.75×10^{-6}	1.0×10^{-14}	1.0×10^{-4}
	292	8.0×10^{-19}	1.0×10^{-12}	8.0×10^{-7}	1.6×10^{-14}	5.0×10^{-5}
50	58	4.7×10^{-17}	5.0×10^{-12}	9.4×10^{-6}	2.6×10^{-13}	1.8×10^{-4}
	107	2.8×10^{-16}	3.5×10^{-11}	8.0×10^{-6}	1.15×10^{-12}	2.4×10^{-4}
	153	8.7×10^{-16}	1.1×10^{-10}	7.9×10^{-6}	2.8×10^{-12}	3.1×10^{-4}
	198	2.2×10^{-15}	2.5×10^{-10}	8.8×10^{-6}	5.2×10^{-12}	4.2×10^{-4}
	241	4.1×10^{-15}	4.6×10^{-10}	8.9×10^{-6}	8.4×10^{-12}	4.9×10^{-4}
102	52	6.0×10^{-16}	4.9×10^{-11}	1.22×10^{-5}	2.7×10^{-12}	2.2×10^{-4}
	97	2.7×10^{-15}	3.5×10^{-10}	7.7×10^{-6}	1.25×10^{-11}	2.2×10^{-4}
	138	1.7×10^{-14}	1.1×10^{-9}	1.55×10^{-5}	2.9×10^{-11}	5.9×10^{-4}
	178	3.1×10^{-14}	2.4×10^{-9}	1.3×10^{-5}	5.25×10^{-11}	5.9×10^{-4}
	217	5.3×10^{-14}	4.5×10^{-9}	1.2×10^{-5}	8.9×10^{-11}	5.95×10^{-4}
305	42	1.75×10^{-14}	1.4×10^{-9}	1.25×10^{-5}	9.0×10^{-11}	1.9×10^{-4}
	79	1.6×10^{-13}	1.0×10^{-8}	1.0×10^{-5}	4.2×10^{-10}	3.8×10^{-4}
	113	6.7×10^{-13}	3.2×10^{-8}	2.1×10^{-5}	1.0×10^{-9}	6.7×10^{-4}
	145	9.7×10^{-13}	7.0×10^{-8}	1.4×10^{-5}	1.8×10^{-9}	5.4×10^{-4}
	176	1.8×10^{-12}	1.3×10^{-7}	1.4×10^{-5}	2.95×10^{-9}	6.1×10^{-4}
560	36	2.4×10^{-13}	7.8×10^{-9}	3.1×10^{-5}	5.7×10^{-10}	4.2×10^{-4}
	69	1.5×10^{-12}	6.2×10^{-8}	2.4×10^{-5}	2.8×10^{-9}	5.35×10^{-4}
	98	4.4×10^{-12}	1.9×10^{-7}	2.3×10^{-5}	6.6×10^{-9}	6.7×10^{-4}
	126	1.0×10^{-11}	4.2×10^{-7}	2.4×10^{-5}	1.2×10^{-8}	8.3×10^{-4}
	152	1.3×10^{-11}	7.5×10^{-7}	1.7×10^{-5}	1.9×10^{-8}	6.8×10^{-4}
940	31	2.9×10^{-12}	3.3×10^{-8}	8.8×10^{-5}	2.7×10^{-9}	1.1×10^{-3}
	59	9.7×10^{-12}	2.5×10^{-7}	3.4×10^{-5}	1.3×10^{-8}	7.5×10^{-4}
	85	2.2×10^{-11}	8.0×10^{-7}	2.75×10^{-5}	3.1×10^{-8}	7.1×10^{-4}
	109	4.4×10^{-11}	1.8×10^{-6}	2.4×10^{-5}	5.7×10^{-8}	7.7×10^{-4}
	132	4.7×10^{-11}	3.2×10^{-6}	1.5×10^{-5}	9.1×10^{-8}	5.1×10^{-4}

BASIC DISTRIBUTION LIST

Technical and Summary Reports

Defense Documentation Center
Cameron Station
Alexandria, VA 22314 (12)

Office of Naval Research
Department of the Navy
Attn: Code 471 (1)
Code 102 (1)
Code 470 (1)

Commanding Officer
Office of Naval Research
Branch Office
495 Summer Street
Boston, MA 02210 (1)

Commanding Officer
Office of Naval Research
Branch Office
536 S. Clark Street
Chicago, IL 60605 (1)

Office of Naval Research
San Francisco Area Office
760 Market Street, Room 447
San Francisco, CA 94102
Attn: Dr. P. A. Miller (1)

Naval Research Laboratory
Washington, DC 20390
Attn: Code 6000 (1)
Code 6100 (1)
Code 6300 (1)
Code 6400 (1)
Code 2627 (1)

Naval Air Development Center
Code 302
Warminster, PA 18974
Attn: Mr. F.S. Williams (1)

Naval Air Propulsion Test Center
Trenton, NJ 08628
Attn: Library (1)

Naval Construction Batallion
Civil Engineering Laboratory
Port Hueneme, CA 93043
Attn: Materials Division (1)

Naval Electronics Laboratory Center
San Diego, CA 92152
Attn: Electron Materials
Sciences Division (1)

Naval Missile Center
Materials Consultant
Code 3312-1
Point Mugu, CA 93041 (1)

Commanding Officer
Naval Surface Weapons Center
White Oak Laboratory
Silver Springs, MD 20910
Attn: Library (1)

David W. Taylor Naval Ship R&D Center
Materials Department
Annapolis, MD 21402 (1)

Naval Undersea Center
San Diego, CA 92132
Attn: Library (1)

Naval Underwater System Center
Newport, RI 02840
Attn: Library (1)

Naval Weapons Center
China Lake, CA 93555
Attn: Library (1)

Naval Postgraduate School
Monterey, CA 93940
Attn: Mechanical Engineering Dept. (1)

Naval Air Systems Command
Washington, DC 20360
Attn: Code 52031 (1)
Code 52032 (1)
Code 329 (1)

Naval Sea System Command
Washington, DC 20362
Attn: Code 035 (1)

Naval Facilities
Engineering Command
Alexandria, VA 22331
Attn: Code 03 (1)

Scientific Advisor
Commandant of the Marine Corps
Washington, DC 20380
Attn: Code AX (1)

Naval Ship Engineering Center
Department of the Navy
CTR BG #2
3700 East-West Highway
Prince Georges Plaza
Hyattsville, MD 20782
Attn: Engineering Materials &
Services Office,
Code 6101 (1)

Army Research Office
Box CM, Duke Station
Durham, NC 27706
Attn: Metallurgy &
Ceramics Division (1)

Army Materials & Mechanics
Research Center
Watertown, MA 02172
Attn: Res. Programs Office
(AMXMR-P) (1)

Air Force Office of Scientific
Research
Bldg. 40
Bolling Air Force Base
Washington, DC 20332
Attn: Chemical Science
Directorate (1)
Electronics & Solid State
Sciences Directorate (1)

Air Force Materials Laboratory
Wright-Patterson Air Force Base
Dayton, OH 45433 (1)

Library
Building 50, Room 134
Lawrence Radiation Laboratory
Berkeley, CA 94710 (1)

NASA Headquarters
Washington, DC 20546
Attn: Code RRM (1)

NASA-Lewis Research Center
21000 Brookpark Road
Cleveland, OH 44135
Attn: Library (1)

National Bureau of Standards
Washington, DC 20234
Attn: Metallurgy Division (1)
Inorganic Materials Division (1)

Defense Metals and Ceramics
Information Center
Battelle Memorial Institute
505 King Avenue
Columbus, OH 43201 (1)

Director
Ordnance Research Laboratory
P.O. Box 30
State College, PA 16801 (1)

Director, Applied Physics Laboratory
University of Washington
1013 Northeast 40th Street
Seattle, WA 98105 (1)

Metals and Ceramics Division
Oak Ridge National Laboratory
P.O. Box X
Oak Ridge, TN 37380 (1)

Los Alamos Scientific Laboratory
P.O. Box 1663
Los Alamos, NM 87544
Attn: Report Librarian (1)

Argonne National Laboratory
Metallurgy Division
P.O. Box 229
Lemont, IL 60439 (1)

Brookhaven National Laboratory
Technical Information Division
Upton, Long Island, NY 11973
Attn: Research Library (1)

SUPPLEMENTARY DISTRIBUTION LIST

Technical and Summary Reports

Dr. W. F. Adler
Effects Technology, Inc.
5383 Hollister Ave.
P.O. Box 30400
Santa Barbara, CA 92105

Dr. G. Bansal
Battelle Memorial Institute
505 King Avenue
Columbus, OH 43201

Dr. S. A. Bortz
IITRI
10 W. 35th Street
Chicago, IL 60616

Dr. J. D. Buch
Prototype Development Assoc., Inc.
1740 Garry Ave., Suite 201
Santa Ana, CA 92705

Dr. B. Budiansky
Harvard University
Dept. of Engineering and
Applied Science
Cambridge, MA 02138

Professor H. Conrad
University of Kentucky
Materials Department
Lexington, KY 40506

Dr. A. Cooper
Case Western Reserve University
Materials Department
Cleveland, OH 44106

Dr. N. Corney
Ministry of Defence
The Adelphi
John Adam Street
London, WC2N 6BB
United Kingdom

Dr. R. Bratton
Westinghouse Research Lab.
Pittsburgh, PA 15235

Professor A. G. Evans
University of California at Berkeley
Department of Materials Science
Berkeley, CA 94720

Professor John Field
University of Cambridge
New Cavendish Laboratory
Cambridge, United Kingdom

Dr. I. Finney
University of California
Berkeley, CA 94720

Mr. A. F. Fyall
Royal Aircraft Establishment
Farnborough, Hants, United Kingdom

Dr. L. M. Gillin
Aeronautical Research Laboratory
P.O. Box 4331
Fisherman's Bend
Melbourne, VIC 3001, Australia

Ms. M. E. Gulden
Solar Turbines International
P.O. Box 80966
San Diego, CA 92138

Professor A. H. Heuer
Case Western Reserve University
University Circle
Cleveland, OH 44106

Dr. R. Hoaglund
Battelle Memorial Institute
505 King Avenue
Columbus, OH 43201

Dr. D. P. H. Hasselman
Dept. of Materials Engineering
Virginia Polytechnic Institute
Blacksburg, VA 24061

Mr. T. Derkus
TRW
Cleveland, OH 44117

Mr. E. Fisher
Ford Motor Company
Dearborn, MI 48121

Dr. P. Gielisse
University of Rhode Island
Kingston, RI 02881

Dr. S. Hart
Naval Research Laboratory
Washington, DC 20375

Professor G. Kino
Stanford University
Palo Alto, CA 94303

Professor R. Roy
Pennsylvania State University
Materials Research Laboratory
University Park, PA 16802

Dr. G. Schmidt
Air Force Materials Laboratory
Wright-Patterson Air Force Base
Dayton, OH 45433

Dr. R. A. Tanzilli
General Electric Company
Reentry & Environmental Systems Division
3198 Chestnut Street
Philadelphia, PA 19101

Dr. S. M. Wiederhorn
Inorganic Materials Division
National Bureau of Standards
Washington, DC 20234

Mr. J. Schuldies
AiResearch
Phoenix, AZ 85010

Dr. N. Tallan
Air Force Materials Laboratory
Wright-Patterson Air Force Base
Dayton, OH 45433

Mr. G. Hayes
Naval Weapons Center
China Lake, CA 93555

Dr. R. Jaffee
Electric Power Research Institute
Palo Alto, CA 94303

Dr. P. Jorgensen
Stanford Research Institute
Poulter Laboratory
Menlo Park, CA 94025

Dr. R. N. Katz
Army Materials & Mechanics Research Center
Watertown, MA 02171

Dr. H. Kirchner
Ceramic Finishing Company
P.O. Box 498
State College, PA 16801

Dr. L. Rubin
Aerospace Corporation
P.O. Box 92957
Los Angeles, CA 90009

Dr. D. A. Shockey
Stanford Research Institute
Poulter Laboratory
Menlo Park, CA 94025

Dr. T. Vasilos
AVCO Corporation
201 Lowell Street
Wilmington, MA 01887

Dr. R. Ruh
Air Force Materials Laboratory
Wright-Patterson Air Force Base
Dayton, OH 45433

Professor G. Sines
University of California, Los Angeles
Los Angeles, CA 90024

Mr. J. D. Walton
Engineering Experiment Station
Georgia Institute of Technology
Atlanta, GA 30332

Dr. B. R. Lawn
Physics Department
University of New South Wales
Kingston, New South Wales
Australia

Dr. Peter Heightman
Dept. 5827, W-5
Detroit Diesel Allison
Division of General Motors
P.O. Box 894
Indianapolis, IN 46206

D. W. Richardson
AiResearch Manufacturing Company
Dept. 93-393/503-4Y
111 South 34th Street
P.O. Box 5217
Phoenix, AZ 85010